AGU PUBLICATIONS

JGR

Journal of Geophysical Research: Solid Earth

RESEARCH ARTICLE

10.1002/2016JB013829

Key Points:
- Friction of rocks depends on slip rate: it follows conventional rate and state during slow slip, yet markedly weakens as slip rates approach seismic speeds
- Using conventional microphysics of creep, we develop a physics-based model for steady state friction at all slip rates
- The model uses independently determined parameters to predict quartz friction experiments at all slip rates

Correspondence to:
E. Aharonov,
einatah@mail.huji.ac.il

Citation:
Aharonov, E., & Scholz, C. H. (2018). A physics-based rock friction constitutive law: Steady state friction. *Journal of Geophysical Research: Solid Earth*, *123*, 1591–1614. https://doi.org/10.1002/2016JB013829

Received 4 DEC 2016
Accepted 4 AUG 2017
Accepted article online 28 DEC 2017
Published online 17 FEB 2018

A Physics-Based Rock Friction Constitutive Law: Steady State Friction

Einat Aharonov[1] and **Christopher H. Scholz**[2]

[1]Institute of Earth Sciences, Hebrew University, Jerusalem, Israel, [2]Lamont-Doherty Earth Observatory, Columbia University, Palisades, NY, USA

Abstract Experiments measuring friction over a wide range of sliding velocities find that the value of the friction coefficient varies widely: friction is high and behaves according to the rate and state constitutive law during slow sliding, yet markedly weakens as the sliding velocity approaches seismic slip speeds. We introduce a physics-based theory to explain this behavior. Using conventional microphysics of creep, we calculate the velocity and temperature dependence of contact stresses during sliding, including the thermal effects of shear heating. Contacts are assumed to reach a coupled thermal and mechanical steady state, and friction is calculated for steady sliding. Results from theory provide good quantitative agreement with reported experimental results for quartz and granite friction over 11 orders of magnitude in velocity. The new model elucidates the physics of friction and predicts the connection between friction laws to independently determined material parameters. It predicts four frictional regimes as function of slip rate: *at slow velocity* friction is either velocity strengthening or weakening, depending on material parameters, and follows the rate and state friction law. Differences between surface and volume activation energies are the main control on velocity dependence. At *intermediate velocity*, for some material parameters, a distinct velocity strengthening regime emerges. *At fast sliding*, shear heating produces thermal softening of friction. At the *fastest sliding*, melting causes further weakening. This theory, with its four frictional regimes, fits well previously published experimental results under low temperature and normal stress.

Plain Language Summary Experiments measuring friction over a wide range of sliding velocities find that the value of the friction coefficient varies widely: friction is high during slow sliding, yet markedly weakens as the sliding velocity rises to seismic slip rates. We introduce a physics-based theory to explain this behavior. Our model assumes friction is controlled by creep at contacts that form between the sliding surfaces. It also assumes that when sliding is fast contacts heat up, and this affects friction profoundly. Our model is able to quantitatively predict, for the first time, reported experimental results for steady state friction at all experimentally measured slip rates. This is done using material parameters that are measured from other experiments, unrelated to friction. The new model may have far reaching implications for understanding friction in general and for earthquake physics in particular.

1. Introduction

The physics controlling frictional resistance during sliding between surfaces has been intensely studied for centuries. It is of particular importance to earthquake physics, as the relation between friction and shearing velocity controls stability of sliding on geological faults and earthquake nucleation, location, and size (e.g., Scholz, 1998). Thus, previous work concentrated on the relation between friction and velocity and between friction and temperature (for reviews, see Marone, 1998; Scholz, 2002). Experimental observations on many geologic materials show that at low slip velocities friction is high (~0.6–0.8) and has only a second-order dependence on velocity. Above a critical velocity friction falls precipitously, as shown in Figure 1 (Di Toro et al., 2011). At intermediate velocities there may be a peak in friction for some materials (e.g., Spagnuolo et al., 2016), as also seen in Figure 1. In addition, friction is observed to change as a function of ambient temperature in most materials (e.g., Blanpied et al., 1995; Chester, 1994; Chester & Higgs, 1992; Lockner et al., 1986; Van Diggelen et al., 2010; Verberne et al., 2015), although not in all (e.g., Boettcher et al., 2007). An important challenge is to combine all these observations into a coherent, physics-based, description of friction as function of the full range of velocity, from slow to very fast, varying normal stress up to a few hundreds of MPa and varying ambient temperature up to the brittle ductile transition. This is basic for understanding earthquake

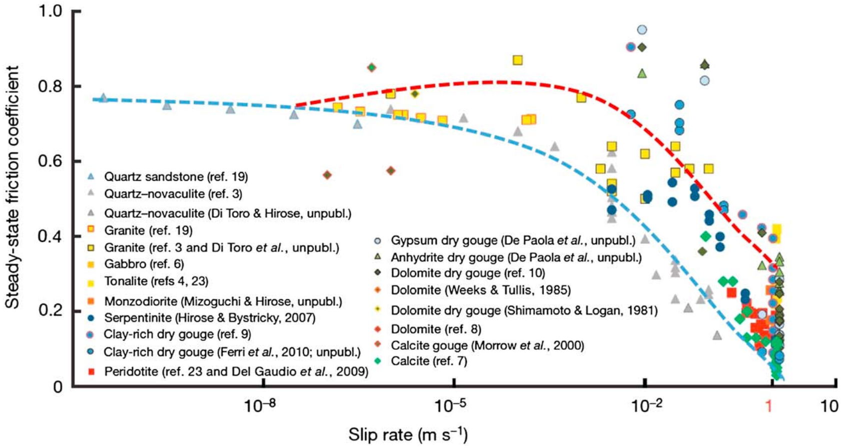

Figure 1. Steady state friction, μ_{ss}, as function of shear velocity, V, in experimental shear in various rocks, adapted from Figure 3 in Di Toro et al. (2011). At slow shearing rate, μ_{ss} is high and varies only slightly with V. When V is greater than ~ mm/s, μ_{ss} starts to decrease strongly with increasing V for all rock and mineral types. Two curves are fit to the data, one with a peak at intermediate V, and another without. Different minerals behave in these two manners.

physics, assessing stability of faults, and predicting the brittle-ductile transition in the Earth (e.g., Marone & Scholz, 1988; Scholz, 1988, 1998).

1.1. Previous Work on the Physics of Friction—Micromechanics of Contacts

In their classic series of works on friction, Bowden and Tabor (1964) suggested that the friction coefficient, μ, measured macroscopically as the ratio of shear to normal stress applied to the surface during sliding, $\mu = \sigma_n/\tau$ actually reflects some averaging of the physical interactions that occur among a multitude of interacting microscopic contacts during sliding (Figure 2a). Bowden and Tabor (abbreviated here as B&T) suggested that the *real area of contact* between surfaces, A_r, is much smaller than the apparent area of the surface, A, and is given by $\sigma_c A_r = W$, where W is the normal load and σ_c is the indentation hardness of the material. Thus, each contact is under a much higher normal stress than the nominal stress σ_n, and the contact stress is $\sigma_c = \sigma_n A/A_r$. If the contacts require a specific shear stress, τ_c, for yielding in shear, then the shear force needed to shear the surface is $F = \tau_c A_r$, and the coefficient of friction becomes $\mu = F/W = \tau_c/\sigma_c$. This idea, of existence and yielding of microscopic contacts as the origin of macroscopic friction, is one of the pillars of present-day understanding of dry friction.

It is by now well established (e.g., Dieterich & Kilgore, 1994; Rubinstein et al., 2004) that indeed shearing surfaces touch at a sparse array of contacts (Figure 2a), that at room temperature constitute $<1\%$ of the apparent area. The main issue is finding the appropriate expressions for τ_c and σ_c, as these are not simply constant values of plastic yield stresses, as initially was assumed. One demonstration of the nonconstancy of contact stresses comes from the observation (Dieterich & Kilgore, 1994) that the real contact area, A_r, grows logarithmically with time of contact, so that σ_c decays logarithmically with contact time. Indeed, static friction, the resistance to initiate sliding from rest, is measured to increase logarithmically with contact time (Dieterich, 1972).

1.2. Previous Work on the Physics of Friction—Rate and State Theory

Beyond the contact-yielding concept of B&T, the empirically based rate and state (R/S) theory was developed to model observations on friction that showed that the macroscopic steady state friction, μ_{ss}, depends logarithmically on slip rate V (Scholz et al., 1972) and on hold time in stationary contacts (Dieterich, 1972). The R/S friction law, in its several variations (Dieterich, 1979; Ruina, 1983) now 30 years old, sparked a revolution in earthquake physics. It allowed us the ability to understand frictional instability in terms of a small number of empirical friction parameters that could be readily measured in the laboratory. From this the gamut of earthquake behavior could be deduced (e.g., Scholz, 1998). For *steady state* sliding R/S can be written as (e.g., Scholz, 1998)

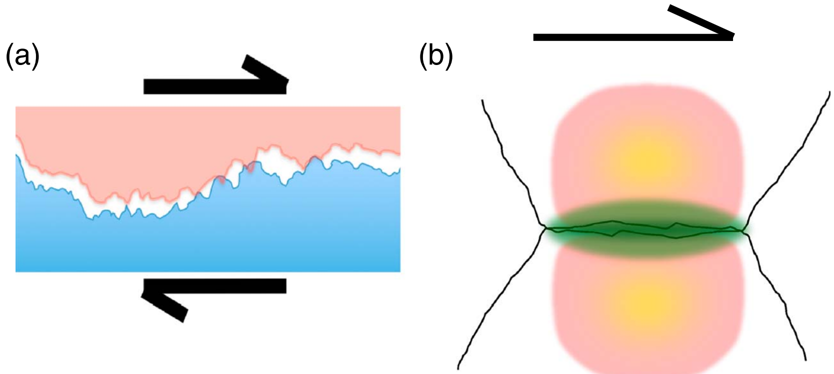

Figure 2. (a) Illustration of shearing rough surfaces, depicting that the real contact area, A_r, is much smaller than the apparent area of contact. (b) Zoom into a single asperity contact. The red fuzzy area depicts a highly compressed region that may undergo internal creep, with the maximum compression area depicted in yellow. This creep, driven by normal stress, may occur by dislocation glide within this region, pressure solution, or subcritical fracture growth, causing asperity convergence and flattening compensated by contact area growth. In contrast, the green region demarcates the contact interface, where shear-activated creep is localized. Note that the two creep processes may be different and that this difference strongly affects friction.

$$\tau = \sigma_n \, \mu_{ss} = \sigma_n \left[\mu^* + (a - b)\ln(V/V^*)\right] \tag{1}$$

The constants μ^* and V^* are often chosen arbitrarily, and the constant coefficients a and b quantify the effect of direct velocity dependence and state dependence of friction, respectively. In this framework, the relative values of a and b control stability of sliding and therefore are suggested to control earthquake nucleation (Dieterich, 1978; Scholz, 1998). Equation (1) was shown by many experiments to provide a good description of sliding friction at slow velocities (e.g., see reviews in Marone, 1998; Baumberger & Caroli, 2006).

R/S is very different in concept from B&T theory, as it was developed as an empirical constitutive relation without considering the physics of contacts. Yet although the $\ln(V/V_*)$ term in equation (1) was introduced empirically by Dieterich (1979, 1978) and Ruina (1983), many studies suggest that it arises from thermally activated creep processes at asperity contacts (e.g., Baumberger, 1997; Baumberger & Caroli, 2006; Brechet & Estrin, 1994; Chester, 1994; Heslot et al., 1994; Nakatani, 2001; Noda, 2008; Putelat et al., 2011; Rice et al., 2001). Since at room temperature real contact area is typically $<1\%$ of the nominal area (e.g., Dieterich & Kilgore, 1994; Rubinstein et al., 2004), assuming 10 MPa applied normal stress, each contact experiences stress of the order of 1 GPa. At such high stress, creep is expected to be exponential in stress and may proceed by one or several of the following physio-chemical mechanisms: stress corrosion, leading to subcritical crack growth (Atkinson, 1987) and static fatigue (Scholz, 1972); Peierls-type mechanisms impeding dislocation glide (Evans & Goetze, 1979; Rice et al., 2001; Tsenn & Carter, 1987) and solution transfer creep (pressure solution) (Nakatani & Scholz, 2004a, 2004b). In friction there are two components of creep that must be considered: normal creep that shortens the contact and increases its area, and creep on contact surfaces that accommodates shear sliding (Figure 2b). Thermally activated creep in both components was used to explain/predict the observed R/S behaviors, for both slow (e.g., Baumberger & Caroli, 2006; Brechet & Estrin, 1994; Li & Rubin, 2017; Nakatani, 2001; Nakatani & Scholz, 2004a, 2004b; Perfettini & Molinari, 2017) and intermediate rate sliding (Bar-Sinai et al., 2014; Noda, 2008).

1.3. Recent Work on the Physics of Friction—High Slip Rate

A different behavior from the R/S logarithmic behavior occurs at high slip rate. Using new high-speed experimental apparatuses, a dramatic weakening was observed at all sliding materials at around $V \sim O(10^{-2})$ m/s, independent of material, as shown in Figure 1. This high-velocity weakening has been attributed to a variety of mechanisms, all of them related to shear heating: (1) "Flash heating" of highly stressed, short-lived, contact asperities. Heated contacts soften and weaken, and even melt at high V (e.g., Beeler et al., 2008; Goldsby & Tullis, 2011; Proctor et al., 2014; Rice, 2006; Yao et al., 2016); (2) chemical/phase changes occurring above a certain temperature: for example, decomposition in carbonates (e.g., Goren et al., 2010; Sulem & Famin, 2009), silica gel formation in quartz (e.g., Goldsby & Tullis, 2002; Kirkpatrick et al., 2013), or antigorite serpentinite transformation into talc (Kohli et al., 2011); (3) thermal pressurization due to shear heating of pore fluids (e.g., Faulkner et al., 2011; Ferri et al., 2010; Goren & Aharonov, 2007, 2009; Goren et al., 2010; Noda & Lapusta, 2013; Rice, 2006); (4) localization and thermo-elastic instabilities (e.g., Braeck & Podladchikov, 2007; Brown & Fialko, 2012; Kelemen & Hirth, 2007; Platt et al., 2014; Siman-Tov et al., 2015), possibly also driven by decomposition (Platt et al., 2015); (5) special behavior of nanograin layers that often cover principle slip zones in faults (e.g., Chen et al., 2013; De Paola et al., 2015; Green et al., 2015; Reches & Lockner, 2010; Siman-Tov et al., 2013, 2015; Verberne et al., 2014, 2014).

Much of the above mentioned work (as well as other work) on high V sliding have been quite successful in explaining steady state friction as a function of velocity. Yet nearly always these studies allowed fitting of free parameters and so did not involve full constraint by material parameters. In addition, none of the above work was able to carry the physics from low to high V, and from low to high ambient temperature and normal stress. They all looked at some window of the velocity, normal stress, and temperature phase space.

To summarize the current state of affairs in theoretical understanding of rock friction: separate theories exist for slow and fast shearing, many based on the Bowden and Tabor concept, and many are fitted somewhat freely. To the best of our knowledge, there is currently no unifying, physics-based model, which may be applied to different minerals, to predict friction across velocities and ambient temperatures. Such a model is needed to predict sliding stability of faults (e.g., Noda & Lapusta, 2013; Scholz, 1998) and the brittle-ductile transition (e.g., Shimamoto & Noda, 2014).

1.4. This Work

The R/S friction laws, being empirical, were rather opaque, lending themselves to various interpretations of the physical processes represented by earthquake behavior and their relationships with the parameters in the laws. It was naively hoped that the friction parameters would be dependent only on the material, so that measurements of these for a few key fault-forming minerals would map out the seismogenic nature of faults in various environments. Laboratory measurements now show that the steady state friction parameters, even for a given mineral type, vary in complex ways with sliding velocity, temperature, normal stress, and with the microstructure formed on the fault sliding surfaces (e.g., Blanpied et al., 1995; Carpenter et al., 2016; Chester & Higgs, 1992; den Hartog et al., 2012; Verberne et al., 2014, 2014, 2015).

These developments make it clear that for further progress to be made a physics-based friction law that incorporates the R/S friction elements needs to be developed. Here we present some basic steps in that direction. We present a single, physics-based, friction law to explain friction observations in rocks, across a wide range of rock types, slip velocities, and temperatures, predicting the data in Figure 1 and similar experimental findings. Our theory models friction at all velocities continuously, from low to high contact temperature regimes, connecting previously proposed physics of contact creep at low contact temperature, to flash heating at intermediate contact temperature and to flash melting/decomposition at high contact temperature. Although our model is general, we apply our results first to quartz and granite, as these materials have currently the largest number of friction data. Also, most of the thermodynamic parameters that appear in our formulation of the friction law can be estimated from independent measurements for quartz. Hence, for quartz-rich rocks we can make quantitative and independent comparisons of theory with friction experiments, rather than relying on data fitting.

Specifically, we show below that our model may explain and predict the following general observations that are not material specific: (a) high friction and second-order material-dependent V dependence at low V. (R/S friction law behavior); (b) material-dependent peak at intermediate V; (c) material independent abrupt thermally induced velocity weakening above a critical V; and (d) all material dependencies result from independently determined variations in material properties.

2. Theory

2.1. Assumption 1: Friction Arises From Creep of Contacts, and Is Predictable From Contact Stresses

We follow B&T, assuming friction arises from interactions of highly stressed contacts of microscopic asperities between surfaces and grains. The contacts exhibit time-dependent shortening and spreading under the applied normal load, so that the asperity height h shortens with time via thermally activated creep driven by the normal stress on the contact, σ_c. Since plasticity maintains volume, their contact area grows as they shorten, thereby reducing the contact stress σ_c. In a similar manner, shearing is assumed to occur at a rate V via thermally activated shear creep, driven by the shear stress on contacts, τ_c. This formalism for the physics of friction has been extensively developed over the last decades (e.g., Baumberger & Caroli, 2006; Brechet & Estrin, 1994; Heslot et al., 1994; Nakatani, 2001; Putelat et al., 2011; Rice et al., 2001). Creep is assumed to depend exponentially on contact stresses τ_c and σ_c (e.g., Chester, 1994; Evans & Goetze, 1979; Tsenn & Carter, 1987). As mentioned above exponential creep represents low-temperature creep such as occurs in subcritical crack growth (e.g., Wiederhorn & Bolz, 1970), Peierls creep (e.g., Ashby & Verrall, 1973), and pressure solution. The application of low-temperature plasticity for asperity creep is also supported by experimental observations of dislocation activation at grain contacts (Boettcher et al., 2007). Thermal activation depends on contact temperature, T_c, and uses the general expression for exponential creep based on rate theory (e.g., Poirier, 1985). Under these assumptions, the equations for the shearing velocity V and contact (asperity) compaction (or convergence) velocity, $\mathrm{d}h/\mathrm{d}t$, are

$$V = V_{s\max} \exp\left(-\frac{Q_s - \tau_c N\Omega_s}{RT_c}\right); \tag{2a}$$

$$\frac{\mathrm{d}h}{\mathrm{d}t} = -V_{n\max} \exp\left(-\frac{Q_v - \sigma_c N\Omega_v}{RT_c}\right), \tag{2b}$$

where N is the Avogadro number, R is the gas constant, and h is the asperity height. $V_{s\max}$ and $V_{n\max}$ are reference, (highest possible), shear and normal creep rates, achieved when contact stresses are at their highest possible value $\tau_c = \tau_c^* = Q_s/N\Omega_s$ and $\sigma_c = \sigma_c^* = Q_v/N\Omega_v$, respectively. Equations (2a)–(2b) describe thermally activated creep in which the deformation is controlled by thermally activated jumps dictated by a pinning potential field with valley depth Q (activation energy) and spacing of valleys of the order of $\Omega^{1/3}$ (activation volume). Equations (2a) and (2b) are basically equations (6) and (12) of Putelat et al. (2011), respectively. It is important to note that activation energy, Q_s, and activation volume, Ω_s, for surface (shear) creep, may differ from bulk volumetric creep parameters, Q_v and Ω_v, which control flattening of the asperity by creep deep within the asperity, as depicted in Figure 2b. (To avoid confusion that may arise from the term "volumetric," we clarify that the asperity flattening creep process occurs at constant volume.) Potentially, different processes could control the flattening and shear deformations. Even under the same process, the application of a von Mises yield criterion predicts a geometrical difference between the resistance to shortening and shear of asperities. In addition, varying water content will change the activation energy as function of distance from the contact. Since shear occurs at the contact interface while flattening occurs within the contact volume, differing dislocation densities, with increased dislocation density near the surface, could affect the different processes. Defect density, related to dislocation density, may also correlate with interstitial water content. The values of activation energies and activation volumes for shear and normal creep will be shown below to control both the base value of the friction coefficient and its velocity dependence.

Although equations (2a) and (2b) are symmetrical, the two dependencies of σ_c and τ_c on shear velocity V are different. This difference is due to the different boundary conditions in the normal and tangential directions: while steady state sliding experiments impose the shear velocity V as a boundary condition, the convergence rate $\mathrm{d}h/\mathrm{d}t$ is not imposed. Its temporal evolution is solved from equation (2b). To solve equation (2b), we assume that contacts in steady state sliding are created and destroyed continuously. Steady state entails that each contact has a lifetime that depends on sliding rate V and contact size d. For each contact the moment it is born is $t = 0$, at which time the height of the contact is h_0, its radius is r_0, and the normal stress on it is σ_c^0. Following Brechet and Estrin (1994), Baumberger and Caroli (2006), and Putelat et al. (2011), we assume constant contact volume during plastic deformation, that is, $r^2 h = r_0^2 h_0$, where r is contact radius at time t. For steady state sliding we assume constant number of equal-sized circular contacts, n, per unit area, so $\sigma_n A = \sigma_c A_r = \sigma_c n\pi r^2$. Thus, $\sigma_c = \sigma_c^0 h/h_0$ and $\mathrm{d}\sigma_c/\mathrm{d}t = (\sigma_c^0/h_0)\, \mathrm{d}h/\mathrm{d}t$. From these, equation (2b) may be rewritten as

$$\frac{\mathrm{d}\sigma_c}{\mathrm{d}t} = -V_{n\max} \frac{\sigma_c^0}{h_0} \exp\left(-\frac{Q_v - \sigma_c N\Omega_v}{RT_c}\right). \tag{2c}$$

We can now integrate (2c) to calculate the contact stress, $\sigma_c(t)$, as function of time since formation of the contact, the thermodynamic variables, and the initial contact stress σ_c^0.

$$\sigma_c(t) = \sigma_c^0[1 - b' \ln(1 + t/t_c)]; \tag{2d}$$

$$b' = \frac{RT_c}{\sigma_c^0 N\Omega_v}\,;\; t_c = b' \frac{h_0}{V_{n\max}} \exp\left(\frac{Q_v - N\Omega_v \sigma_c^0}{RT_c}\right) \tag{2e}$$

The characteristic time constant, $t_{c,}$ was defined as the “cutoff time” by Berthoud et al. (1999), and its physical meaning will be detailed in section 6.

In order to evaluate σ_c, the contact stress at time t = 0, $\sigma^0_{c,}$ is needed. σ_c^0 was assumed in previous theoretical analysis (Putelat et al., 2011) to be equal to $\frac{Q_v}{N\Omega_v}$. However, there are several reasons to think that $\sigma_c^0 = \mathrm{B}\frac{Q_v}{N\Omega_v}$, with $0 < B < 1$:

1. There is no physical argument that dictates that the two values—σ_c^0 the indentation hardness at time of contact initiation and the thermodynamic parameter, $\frac{Q_v}{N\Omega_v}$, should be equal.
2. An assumption of $B = 1$, that is, $\sigma_c^0 = \frac{Q_v}{N\Omega_v}$, forces contact-normal creep rate ($\mathrm{d}h/\mathrm{d}t$ in equation (2b)) at $t = 0$ to be independent of temperature, while it is reasonable to expect it to be thermally activated—to vanish at $T_c = 0$ and increase to maximum rate, $V_{n\max,}$ at $T_c \rightarrow \infty$. This argument leads to $0 < B < 1$.
3. Using $\sigma_c^0 = \frac{Q_v}{N\Omega_v}$ (i.e., B = 1) in equation (2e) predicts two things: that the cutoff time t_c grows linearly with T_c (due to b′), and that the activation energy for t_c, E_c, is 0. In contrast, assuming $B < 1$ dictates that t_c is thermally activated, with an activation energy $E_{\mathrm{tc}} = (1 - B)Q_v$. In this case t_c has an exponential dependence on $1/T$, in agreement with the experimental findings of Nakatani and Scholz (2004a, Figure 7).
4. The indentation hardness at time $t = 0$, σ_c^0, and thus also B, are expected to decrease with ambient temperature, following Evans (1984), who measured that indentation hardness of quartz drops by 30–50% as temperature is raised from 0 to 500°C. So not only is $B < 1$, it is even not a constant. Instead, it drops with the ambient temperature T_0.
5. In addition to depending on T and stress, creep rate $\mathrm{d}h/\mathrm{d}t$ will also depend on the dislocation density. Creep laws are derived for steady state, but the initial creep response will occur with dislocation density much less than that at steady state, allowing much faster initial creep owing to a lack of “work hardening.” It is common to observe rapid transient creep during dislocation creep (i.e., lower yield strength than steady state strength). Thus, the assumption $\sigma_c^0 = \frac{Q_v}{N\Omega_v}$, that is, that the indentation hardness has the highest possible value at $t = 0$ clearly overestimates σ_c^0.

We now rewrite equations (2a)–(2e) doing two things—first, inverting equation (2a) to obtain τ_c as function of V, providing equation (3b). Second, use the contact lifetime in steady state sliding rate $t = d/V$ (where $d = 2r$ is the contact diameter), in place of time in equation (2d) (see, e.g., section 2 of Baumberger & Caroli, 2006 for justification of this approximation):

$$\sigma_c(t) = \sigma_c^0\left(1 - b' \ln\left(1 + \frac{d}{Vt_c}\right)\right) \tag{3a}$$

$$\tau_c(t) = \tau_c^*\left(1 + a' \;\ln\left(\frac{V}{V_{s\max}}\right)\right) \tag{3b}$$

$$\frac{A_r}{A} = \frac{\sigma_n}{\sigma_c^0} \frac{1}{\left(1 - b' \ln\left(1 + \frac{d}{Vt_c}\right)\right)} \tag{3c}$$

$$a' = \frac{RT_c}{Q_s}\,;\; b' = \frac{RT_c}{BQ_v}\,;\; \sigma_c^0 = \frac{Q_v B}{N\Omega_v}\,;\; \tau_c^* = \frac{Q_s}{N\Omega_s}\,;\; E_{\mathrm{tc}} = Q_v - N\Omega_v \sigma_c^0 = (1 - B)Q_v \tag{3d}$$

$$t_c = b' \frac{d}{V_{n\max}} \exp\left(\frac{E_{\mathrm{tc}}}{RT_c}\right) = t_{cr} \frac{T_c}{T_{\mathrm{cr}}} \exp\left(-\frac{E_{tc}\,\Delta Tc}{R\,T_c\,T_{\mathrm{cr}}}\right); \tag{3e}$$

Equations (3d) and (3e) provide the constants for calculating contact stresses σ_c and τ_c in equations (3a) and (3b). Equations (3a)–(3e) are the same as in the above mentioned previous studies (see Putelat et al., 2011 for detailed derivation, and Nakatani and Scholz (2004b), derivation of their equation (13)), except for the newly added prefactor $B < 1$, the outcome of which is the newly defined E_{tc}.

Assuming a reference cutoff time t_{cr} at a reference temperature T_{cr}, and $\Delta T_c = T_c - T_{\mathrm{cr}}$, and dividing t_c by this reference cutoff time t_{cr}, provides equation (3e) as another formulation for the cutoff time, with more easily obtained parameters than those in equation (2e). Note that the physics behind this formalism dictates that constants $V_{s\max}$ and $V_{n\max}$ are much greater than the sliding rate V, as they represent the physical upper limit to the creep rate in the respective creep processes. Also note from equation (3b) that τ_c^* provides the value of the highest possible shear stress. This maximum shear stress is attained not at the time of contact initiation (i.e., τ_c^* is not attained at the same time as σ_c^0) but is only achieved when sliding is at the highest possible shear velocity, $V_{s\max}$.

Equation (3c) provides the real contact area, calculated from equation (3a) using $\sigma_n A = \sigma_c A_r$. The behavior predicted by (3c), namely logarithmic growth of real contact area with time, is observed in microindentation experiments by Scholz and Engelder (1976) in both olivine and quartz.

The steady state friction coefficient is easily obtained from equations (3a)–(3e) via

$$\mu_{ss} = \frac{\tau}{\sigma_n} = \frac{\tau_c}{\sigma_c} = \frac{\tau_c^*\left(1 + a' \ \ln\left(\frac{V}{V_{s\max}}\right)\right)}{\sigma_c^0\left(1 - b' \ln\left(1 + \frac{\mathrm{d}}{Vt_c}\right)\right)} \tag{4a}$$

where σ_n and τ are the applied normal and shear stress on the surface.

From the full steady state friction one may obtain the rate and state equation by Taylor expanding equation (4a), assuming that the $b' \ln\left(1 + \frac{\mathrm{d}}{Vt_c}\right)$ term is small:

$$\mu_{ss} \sim \mu_0 + a^* \ln\left(\frac{V}{V_{s\max}}\right) + b^* \ln\left(1 + \frac{d}{t_c V}\right) + \frac{a^* b^*}{\mu_0} \ \ln\left(\frac{V}{V_{s\max}}\right) \ln\left(1 + \frac{\mathrm{d}}{t_c V}\right) + \frac{1}{\mu_0}\left(b^* \ln\left(1 + \frac{d}{t_c V}\right)\right)^2 + \ldots \tag{4b}$$

$$a^* = a' \ \mu_0 = \mu_0 \frac{RT_c}{Q_s}; \ b^* = b' \mu_0 = \mu_0 \frac{RT_c}{BQ_v}; \ \mu_0 = \frac{\tau_c^*}{\sigma_c^0} = \frac{Q_s}{BQ_V}\frac{\Omega_V}{\Omega_S}, \tag{4c}$$

where the coefficients a', b', and t_c are given by equations (3d) and (3e). Equation (4b) contains first- and second-order terms. The above Taylor expansion required that the whole b' term (not only the b' coefficient) is <1, which indeed is always true. Yet the b' term may in some cases be large enough to necessitate retaining the second-order terms, as discussed below. The first three terms of equation (4b) constitute the regularized rate and state equation as derived in many previous works (see, e.g., Baumberger & Caroli, 2006, equation (32)).

We may further approximate equation (4b) for the slowest slip regime (where $V \ll \frac{d}{t_c}$), using the approximation that in this regime $\ln\left(1 + \frac{d}{t_c V}\right) \sim \ln\left(\frac{d}{t_c V}\right)$. In this regime also $|\ln V| \gg 1$, so we keep the $\ln^2$ terms.

$$\mu_{ss} \sim \mu^* + \ln(V)\left[(a^* - b^*) + \frac{a^* b^*}{\mu_0} \ \ln\left(\frac{dV_{s\max}}{t_c}\right) - \frac{2b^{*2}}{\mu_0} \ln\left(\frac{d}{t_c}\right)\right] - (\ln V)^2 \frac{b^*}{\mu_0}(a^* - b^*) + \ldots \tag{4d}$$

where in equation (4d) we defined base level friction, μ^*,as

$$\mu^* \sim \mu_0 - a^* \ln(V_{s\max}) + b^* \ln\left(\frac{d}{t_c}\right) + \text{higher-order terms}\ldots \tag{4e}$$

And μ_0 is defined in equation (4c). Equation (4d) emerges as a rate and state description of steady state friction at the low slip rate limit, recapturing equation (1):

$$\mu_{ss} \sim \mu^* + \ln(V)(a - b) + \left(\text{terms of order } b^{*2} \ln^2 V \text{ and higher}\right), \tag{4f}$$

where the friction parameters a and b in equation (1) emerge as a combination of material parameters:

$$a = a^*\left(1 + \frac{b^*}{\mu_0} \ln\left(\frac{dV_{s\max}}{t_c}\right)\right) \quad ; \quad b = b^*\left(1 + 2\frac{b^*}{\mu_0} \ln\left(\frac{d}{t_c}\right)\right). \tag{4g}$$

and a^* and b^* are defined in equation (4c). The fact that a and b represent defined physical parameters is discussed at length in previous work (e.g., Bar-Sinai et al., 2014; Baumberger & Caroli, 2006; Noda, 2008; Putelat et al., 2011; Rice et al., 2001). Note, however, that in contrast to previous theoretical derivations, the R/S parameters a and b in equation (4g) include second-order corrections. These second-order corrections are crucial if $Q_s = Q_v$ and $B \approx 1$, since then $a^* = b^*$ (see equation (4c)), the first-order terms cancel out, and only the second-order terms remain in equations (4f) and (4g). The corrections may be very important in other cases as well. The reason is that although b^* is small, of $O(10^{-2})$, due to the large logarithmic term (absolute values ranging between 10 and 30 depending on parameters), the second-order corrections may change a and b values by up to 50%. For the same reason, at very small V, one must also include the $\ln^2 V$ term. In addition, the values of a^* and b^* grow linearly with contact temperature (equation (4c)).

For all these reasons we calculate friction in our model directly from $\frac{\tau_c}{\sigma_c}$, that is, from equation (4a), and not from equations (4b) or (4f). Yet since the approximations of equations (4b) and (4f) are valid for some velocity and parameter ranges we use them in section 6 for analysis and to obtain insights into the frictional behaviors.

As a consequence of equations (4a)–(4g), contact temperature and friction are strongly coupled. During sliding, contact temperature, T_c, rises due to frictional shear heating, which is controlled by the friction coefficient from equation (4a). On the other hand, rising T_c changes frictional resistance via prefactors a, b, and t_c in equations (3a)–(3e) and (4a). Thus, T_c and μ_{ss} are coupled, and this coupling is crucial in controlling intermediate to high-speed friction, as demonstrated recently in the experiments of Yao et al. (2016).

2.2. Assumption 2: Steady State Temperature and Friction

As seen in Figure 1 of DiToro et al. (2011), high-velocity friction weakens with slip and reaches a steady state after sliding a distances D_{th}. This high-velocity weakening is thermally induced, by various mechanisms including (but not limited to) flash heating, decomposition in carbonates, melting in quartz, and thermal pressurization. All of those mechanisms require a steady frictional heat production to be maintained, which results in negative feedback such that steady states in friction and temperature are simultaneously attained.

To calculate the steady state contact temperature, T_c, we follow previous formulations (e.g., Beeler et al., 2008; Noda, 2008; Rice, 2006) and assume that sliding contacts undergo "flash heating," via shear heating that takes place during short "contact lifetimes." Flash heating of contacts elevates T_c by amount δT above the average temperature of the surface, T_s, which also increases during sliding. Steady state contact temperature T_c is thus approximated by the sum of the mean surface temperature after sliding distance D_{th} (DiToro et al., 2011, equation (1)), $T_s = T_0 + \frac{\tau_c}{\rho C}\frac{\sigma_n}{\sigma_c}\sqrt{\frac{VD_{\mathrm{th}}}{\pi\alpha}}$, plus flash heating contributions on contacts, $\delta T = \frac{\tau_c}{\rho C}\sqrt{\frac{Vd}{\pi\alpha}}$, (Rice, 2006, equation (3)), where T_0 is ambient temperature, α is thermal diffusivity coefficient, C is heat capacity, and ρ is density of the material:

$$T_c = T_s + \delta T = T_0 + \frac{\tau_c}{\rho C}\sqrt{\frac{V}{\pi\alpha}}\left[\sqrt{d} + \frac{\sigma_n}{\sigma_c}\sqrt{D_{\mathrm{th}}}\right] \tag{5}$$

At high enough sliding velocity, equation (5) predicts contact temperatures T_c that exceed the phase transition temperature of the particular mineral, in this case the melting temperature in quartz (T_m). Yet thermodynamic considerations predict that the temperature at the contacts will remain at the phase boundary, that is, $T_c = T_m$, even if V increases. To maintain T_c at T_m with increasing V, equation (5) that predicts shear stress at contact must follow $\tau_c \sim 1/\sqrt{V}$, since

$$\tau_c^m(V) = \rho C\sqrt{\pi\alpha}\left(T_{\mathrm{melt}} - T_0\right)\Big/\left(\sqrt{V}\left[\sqrt{d_m} + \frac{\sigma_n}{\sigma_c^m}\sqrt{D_{\mathrm{th}}}\right]\right), \tag{6}$$

where we assume d_m and σ_c^m are constant and independent of V. Note that equation (5) was originally developed for "flash heating" during premelting (Rice, 2006), yet it was used successfully to also model the phase change during flash melting (Beeler et al., 2008), despite the approximations involved. Since the main focus of this paper is the premelting stage, the approximation of equation (6) is considered satisfactory and we leave more accurate theoretical representations of the melting regime for future work.

3. Parameter Values

To solve coupled equations (3a)–(3e) and (5) (and also equation (6) once melting sets on), we constrain values of the parameters used, via previous independent measurements. All of these parameters are thermodynamic or mechanical parameters of the mineral. Here we concentrate on the mineral quartz for which many of those parameters are well determined. Table 1 outlines their values.

Activation energies Q_v and Q_s, values are constrained to within a factor of less than 2, which is not too bad given that the processes that control the creep are not well constrained. We expect a difference between Q_v and Q_s: Shear deformation involves very high strain in a surface layer whereas the surface-normal deformation involves presumably a much smaller strain, which occurs within the bulk of the asperity volume (Figure 2b). These two processes may result in different defect structures, and especially the high dislocation density can result in strengthening of the surface layer. Additionally, these two processes may result in different interstitial water content that can greatly affect the activation energy of quartz. The variability of Q as function of water content was measured by Mainprice and Jaoul (2009), who found dislocation creep activation energy in quartzite ranged between 185 kJ/mol for vacuum dried and 151 kJ/mol for 0.4 wt % water added samples. Similarly, Jaoul et al. (1984) measured a 25% decrease in activation energy as water content in Heavitree Quartzite was raised from 0.1 to 0.5% weight. Thus, activation energy for internal deformation within the asperity, which controls the contact-normal creep, Q_v, and surface deformation that controls shear creep on the asperity surface, Q_s, needs not be equal. Activation energies cited previously in the literature do not distinguish between volume and surface processes and do not even discuss the possibility for such difference. Q associated with quartz friction usually ranges between 150 and 250 KJ/mol (Kirby & Kronenberg, 1987; Mainprice & Jaoul, 2009; Nakatani, 2001; Rice et al., 2001), but values ranging between 90 and 500 KJ/mol have also been suggested (Nakatani, 2001). Here we thus used values ranging between 150 and 280 KJ/mol.

Similarly, volumetric and surface activation volumes, Ω_v and Ω_s, respectively, are not precisely known and need not necessarily be equal. They again are expected to reflect specific defect structures and process, but values have not been suggested in connection to any specific physical process. Activation volumes are of the size of atomic volumes. Estimates for Ω for quartz friction vary up to 50%, ranging between $(0.37\ \text{nm})^3 = 5 \times 10^{-29}\ \text{m}^3$ (Nakatani, 2001) and $5 \times (0.25\ \text{nm})^3 = 7.8 \times 10^{-29}\ \text{m}^3$ (Rice et al., 2001).

To calculate cutoff times t_c (equation (3e)), one needs either $V_{n\max}$ or a reference cutoff time, t_{cr}, at a reference contact temperature, T_{cr}. t_{cr} values have been experimentally measured, while there is little knowledge of $V_{n\max}$. Room temperature t_{cr} was measured in experiments to range from 1 s (Dieterich, 1972, 1978) to 10,000 s (Nakatani & Scholz, 2004a), with the latter attributed to timescales of pressure solution. In addition, Nakatani and Scholz (2004b) measured t_c as function of T_0 and found t_c is thermally activated, with an activation energy in quartz of $E_{\text{tc}} = 58$ KJ/mol. We can use this measured E_{tc} to constrain also the prefactor B: from equation (3c), $E_{\text{tc}} = (1 - B)Q_v$, so that assuming $Q_v = 280$ KJ/mol and $E_{\text{tc}} = 58$ KJ/mol gives $B{\sim}0.79$, while assuming $Q_v = 170$ KJ/mol with this E_{tc} gives $B{\sim}0.66$. These constraints on B should be used cautiously, due to the fact that this value of E_{tc} was measured during pressure solution. E_{tc} is probably different in the experiments that measured $t_{\text{cr}}{\sim}1$ s, since the controlling process is different, but we do not know this for certain as E_{tc} was not measured there.

An independent additional constraint on prefactor B comes from the value of yield stress, σ_c^0. Optical measurement of asperity contact sizes (Dieterich & Kilgore, 1994, 1996) on various materials including soda-lime and quartz suggests that $\sigma_c^0{\sim}0.2G$, or even larger, where G is shear modulus. This value is consistent with an estimate by Boitnott et al. (1992) and with microhardness indentation strengths measured by Dieterich and Kilgore (1994) (as interpreted by Rice et al., 2001). Using $G = 31$ GPa for quartz, this estimate suggests σ_c^0 ~6 GPa, and using $Q_v = 250$ KJ/mol and $\Omega_v = 5 \times 10^{-29}\ \text{m}^3$ in $\sigma_c^0 = \frac{Q_v B}{N\Omega_v}$ then predicts $B{\sim}0.72$. A lower activation energy, $Q_v = 170$ KJ/mol gives higher value for B, $B > 0.9$. However, high B values and low Q_v values would dictate a low $E_{\text{tc}} < 20$ KJ/mol (according to equation (3e)). We therefore use the following ranges: $Q_v = 220 \pm 70$ KJ/mol and $B{\sim}0.85 \pm 0.1$, consistent with all experimental constrains known today for E_{tc}, σ_c^0, and Q_v. This constrains E_{tc} to be between 10 and 75 KJ/mol.

The value of B quoted above is for room ambient temperature, yet σ_c^0 and B should be a function of T_0. Evans (1984) showed that indentation hardness of quartz, that is, yield stress, drops by 30–50% as T_0 increases from

Table 1
Table of Parameters, Definitions, and Values

Parameter	Symbol	Values	Units	Ref
Volume activation volume	Ω_v	$(5–7.8) \times 10^{-29}$	m^3	Nakatani (2001) and Rice et al. (2001)
Surface activation volume	Ω_s	$(5–7.8) \times 10^{-29}$	m^3	Nakatani (2001) and Rice et al. (2001)
Volume activation energy	Q_v	150–280	KJ/mol	Nakatani (2001), Rice et al. (2001), and Mainprice and Jaoul (2009)
Surface activation energy	Q_s	150–280	KJ/mol	Nakatani (2001), Rice et al. (2001), and Mainprice and Jaoul (2009)
Prefactor	B	0.74–1	-	Here
Contact diameter	d	$0.1–15 \times 10^{-6}$	m	Beeler et al. (2008)
Maximum shear rate	V_{smax}	Here 0.5 c_s		Noda (2008) and Rice et al. (2001)
Shear wave velocity	c_s	3,750	m/s	www.quartz.com
Reference cutoff time, room T	t_{cr}	$10^0–10^6$	s	Dieterich (1972) (1978) and Nakatani and Scholz (2004a)
Cutoff time	t_c		s	From equations (3a)–(3d)
Activation energy for t_c	E_{tc}	20–75 (calculated by equation (3c))	KJ/mol	Nakatani and Scholz (2004a)
Thermal equilibration distance	D_{th}	$= k\sigma_n{}^q$, here assume $k = 5$, $q = -1$.	m	Di Toro et al. (2011) and Di Toro et al. (2004)
(Pre) melting temperature	T_m	1270–1670	K	Rice (2006)
Ambient temperature	T_0	300	K	Imposed
Heat capacity	C	$730 \times (1.7–200/T_c)$	J/Kg/K	Fitting Figure 4 of Vosteen and Schellschmidt (2003)
Thermal diffusivity	α	$= \alpha_0 \times 10^{-4}/T_c - 0.5 \times 10^{-7}$; $\alpha_0 = 0.8–5$	m^2/s	Fitting Figure 4 of Hanley et al. (1978), assuming 1 order of magnitude reduction of α by porosity
Density	ρ	2,650	Kg/m^3	
Contact temperature	T_c	300–2000	K	Calculated from equation (5)
Shear rate	V	$10^{-11}–1$	m/s	Imposed
Applied normal stress	σ_n	5	MPa	Imposed
Steady state friction coef	μ_{ss}	0.01–1	-	Calculated from equations (3a)–(3d)
Contact shear stress	τ_c	(0.01–0.18) G	MPa	Calculated from equations (3a)–(3d)
Contact normal stress	σ_c	(0.1–0.22) G	MPa	Calculated from equations (3a)–(3d)
Viscous shear coefficient	a	See Table 2	-	Calculated from equations (4a)–(4g)
Contact growth coefficient	b	See Table 2	-	Calculated from equations (4a)–(4g)
Avogadro number	N	6×10^{23}	1/mol	
Gas constant	R	8.314	J/mol/K	
Shear modulus	G	31×10^9	Pa	

0 to 500°C. To represent this effect, we use $B(T_0) = B_r\exp(-0.0006(T_0 - T_r))$, where B_r is B at room temperature, so that σ_c^0 drops with ambient temperature T_0 following the trend in Figure 5 of Evans (1984).

Another parameter is the upper limit for shear rate, V_{smax}. The maximum value of V_{smax} has been equated to the natural vibration frequency of atoms in a mineral lattice and linked to the shear wave velocity c_s (Rice et al., 2001). Noda (2008) uses physical arguments to state that V_{smax} is close to this limit of c_s. Since V must be smaller than V_{smax} for the creep physics in equation (2) to hold, and since we use this creep physics across all V, we shall henceforth use $V_{smax} = 0.5c_s$. However, we note that since V_{smax} is under the ln, its exact value is probably not crucial.

The contact diameter is assumed at the time of contact initiation to be $d_0 = 0.1–15$ μm (Beeler et al., 2008). It then depends on slip rate via the constant load assumption: $\frac{d^2}{d_0^2} = \frac{\sigma_c^0}{\sigma_c}$. At low slip rates d remains close to d_0 (within a factor of 1.3). Significant changes in d are only expected at higher ambient temperatures and normal stress, when the real area of contact increases appreciably. The value of d (together with the thermal parameters), controls the amount of shear heating that takes place during contact lifetime. Small d pushes the thermal softening transition to higher slip rates.

Thermal parameters are needed for equations (5) and (6): From experiments at high slip rate, the thermal equilibration distance, $D_{th,}$ is found to drop with applied normal stress, for all rock types, following an empirical relationship (Di Toro et al., 2011) where $D_{th} = k\,\sigma_n{}^{-q}$, and constants k and q depend on material. For lack of better constrains on k and q, we assume $k = 5$ and $q = 1$, which using the empirical relationship above predict

D_{th} = 1 m and 1 cm at 5 Mpa and 400 MPa, respectively, fitting on the one end results from 5 MPa shear experiments on novaculite (Figure 2 of Di Toro et al., 2004) and at the other end providing D_{th} of order of 1 cm at $\sigma_n > 200$ MPa (Di Toro et al., 2011).

Table 2

Summary of Variables Used in Runs

Run variable	1a	1b	1c	1d	2	3	4	5	6	7	8
$\Omega_v(10^{-29}\ \mathrm{m}^3)$	5	5	5	7	6.8	5	5	5	5	5	5
$\Omega_s(10^{-29}\ \mathrm{m}^3)$	5	5	5	6.2	6.0	7.8	7.8	7.8	6.8	7.8	7.8
Q_v(KJ/mol)	200	150	200	150	260	230	240	230	240	230	150
Q_s(KJ/mol)	200	150	200	150	210	280	270	280	260	280	185
B	1	1	1	1	0.9	0.9	0.89	0.9	0.8	0.9	0.74
t_{cr}(s)	1	1	10^4	1	2	1	2	1	5000	1	50
T_m(K)	1270	1270	1270	1670	1670	1270	1370	1670	1270	1270	1370
α_0 (m^2/s)	0.8	0.8	0.8	1.2	1	2	1	1	2	0.8	1
d (μm)	1	1	1	0.1	10	1	10	10	1	15	3
a^* (equation (4b))	0.012	0.017	0.012	0.017	0.0121	0.0077	0.0075	0.0077	0.0096	0.0077	0.0135
b^* (equation (4b))	0.012	0.017	0.012	0.017	0.0108	0.0104	0.0094	0.0096	0.0132	0.0104	0.0225
a^*-b^*	0	0	0	0	0.0013	−0.0027	−0.002	−0.002	−0.0036	−0.0027	−0.009
a (equation (4f))	0.011	0.015	0.009	0.0145	0.0115	0.0074	0.0071	0.0071	0.0077	0.0074	0.0107
b (equation (4f))	0.008	0.009	0.005	0.008	0.008	0.0079	0.0072	0.0075	0.0054	0.008	0.0058
a-b	0.003	0.006	0.004	0.007	0.003	−0.0005	−0.0001	−0.0004	0.0023	−0.0005	0.005
$V_c = d/t_{cr}$ (m/s)	10^{-6}	10^{-6}	10^{-10}	10^{-7}	5×10^{-6}	10^{-6}	5×10^{-6}	10^{-5}	2×10^{-10}	1.5×10^{-5}	6×10^{-8}

Note. a, b, a^*, and b^* (equations (4a)–(4f)) are calculated at room temperature.

Additional Thermal Parameters Are C, ρ, and α. The thermal diffusivity for quartz is $\alpha = 7 \times 10^{-6}$ m^2/s at room temperature; however, the fault and gouge zone porosity reduces this diffusivity by up to an order of magnitude (Gibert & Mainprice, 2009, Figure 8; Siman-Tov et al., 2015). Porosity is important both for "asperity-scale heating" (i.e., the flash heating term in equation (5)) and for the "fault-scale heating" (i.e., the mean surface temperature term in equation (5)): at the fault-scale heat diffuses within the broken and porous fault zone structure. Also at the asperity scale, each asperity is surrounded by a void filled with gas or fluid, that is, heat is diffusing in a very porous medium. Thus, we assume 1 order of magnitude reduction in α due to porosity (see Table 1 for equation). In addition, α drops with temperature (Vosteen & Schellschmidt, 2003), while the heat capacity, C, increases. We fit the thermal dependence of α of quartzite from Hanley et al., (1978, their Figure 4). Density, ρ, is taken constant (Vosteen & Schellschmidt, 2003). Table 1 reports the equation we fitted to the C variation with temperature shown in Vosteen and Schellschmidt (2003). Another parameter is the melting temperature, T_m, that for quartzite is ~ 1670°C. Rice (2006) uses a "weakening temperature" that could be equated with T_m, yet suggests it is lower than melting, 1000–1400°C, representing weakening due to premelting. We consider all these values in our various calculations.

4. Method

For accuracy we calculate friction from the full friction equation, equation (4a). We solve equations (3a)–(3e), (4a), (5), and (6) numerically, seeking a coupled dynamic steady state solution for contact stresses σ_c and τ_c and contact temperature T_c by iterative solutions using a Matlab subroutine that we wrote.

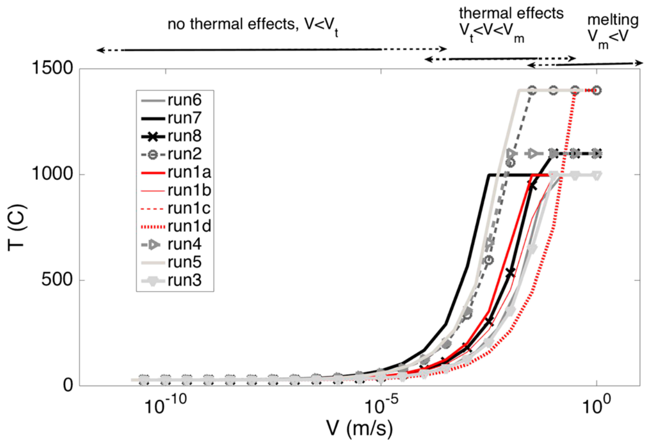

Figure 3. Model calculated steady state contact temperature (T_c) for quartz/granite sliding at room temperature and σ_n = 5 Mpa, as function of slip rate V. We present 11 runs, each using different parameter values within the independently predicted range (see Table 2). For low V, T_c remains at the ambient T. Increasing V brings about two transitions: At V_t and at V_m. V_t is the velocity at which marked heating begins, ~10^{-5}–10^{-4} m/s. At V_m, which varies between 10^{-3} and 10^{-1} m/s, contacts reach melting temperature, T_m, capping the curves at $T_c = T_m$ for any $V > V_m$. The values of the transition velocities V_t and V_m depend primarily on thermal diffusivity and contact size: V_t and V_m in runs 1b, 1d, 3, 6, and 8 are high since these runs have small contacts and/or high diffusivity. Note that runs 1d, 2, and 5 used higher T_m to illustrate the negligible effect that the value of T_m has on V_t and V_m.

In our code the solution converges from the same reason that we propose a dynamic steady state: Negative feedbacks ensure that steady states in friction and temperature are coupled and are reached simultaneously. If τ_c rises it increases T_c via shear heating (equation (5)). The increase in T_c reduces τ_c via prefactor a', in equation (3d). The reduction in τ_c then reduces shear heating and so reduces T_c in equation (5), and so on.

An important deviation from this procedure is taken at high sliding velocity, when intense shear heating produces a steady state T_c that exceeds T_m. In this case equation (6) gives contact stress, τ_c^m, that maintains $T_c = T_m$ while sliding at velocity V.

The present analysis uses velocity V ranging between 10^{-11} and 1 m/s, calculating steady state T_c, τ_c, σ_c, and μ_{ss} as function of shear velocity V for sliding quartz, using 11 different combinations of material parameters, within the range stated in Table 1. All runs were run at room temperature, T_0 = 300 K and normal stress σ_n = 5 Mpa. The parameters used for each of the runs are given in Table 2. The first four runs, runs 1a–1d, use $Q_v = Q_s$ and B = 1. These are "control runs". Runs 2–8 have variable Q_v, Q_s, and B.

5. Results

5.1. Contact Temperature

The first interesting result is the steady state contact temperature, T_c, versus sliding velocity, shown in Figure 3. All runs show three regimes of contact temperature behavior with similar transitions between regimes: at V smaller than a *critical thermal velocity* V_t ~10^{-5}–10^{-4} m/s, no substantial shear heating occurs, so T_c ~T_0. For $V > V_t$ marked heating occurs. At a higher, second critical velocity, $V_m = 10^{-3}$–10^{-1} m/s, T_c reaches T_m, the melting temperature. The very sudden and precipitous temperature rise at the contact scale between V_t and V_m explains why V_m is essentially independent of the value of the melting temperature, T_m (on a curve like that a difference in melting temperatures matters little), as seen by comparing runs 1b and 1d, which have different T_m, yet similar V_m. The critical velocities, V_t and V_m, depend primarily on thermal diffusivity and contact size: runs 2 and 7 show early onset of heating and melting due to relatively large contacts (see Table 2). Runs 1d and 6 show delayed onset of shear heating due to their relatively small contacts and/or high thermal diffusivity.

5.2. Contact Stresses

The combined effect of the parameters in Table 2 and the imposed slip rate, V, controls the value of contact-scale stresses, τ_c and σ_c, shown in Figures 4a and 4b.

The range of "play" in the values of the material parameters, especially the activation energies that may be differ by 100% between runs, and the value of B, which varies by 25% between runs, allows for a range of stress values to emerge, shifting curves up and down. Note the low values of τ_c and σ_c in runs 8, 1b, and 1d, due to the lower activation energies used in those runs, representing the lower end of the allowed range (see Tables 1 and 2). τ_c and σ_c are also affected by Ω_v and Ω_s (equation (3d)), which is why run 1b shows higher stresses than run 1d.

Contact shear stress (Figure 4a) increases with V in all runs until thermal softening begins at $V > V_t$. Contact normal stress (Figure 4b) increases in all runs until $V = V_c = d/t_c$ (V_c for each run noted by arrows). For $V > V_c$ normal stress saturates and remains constant even when shear heating occurs ($V > V_t$). Contact area, A_r, is shown in Figure 4c to decrease in all runs with V until $V = V_c$. For $V > V_c$, A_r saturates and remains at an approximately constant value, the value of contact area at the time of contact initiation.

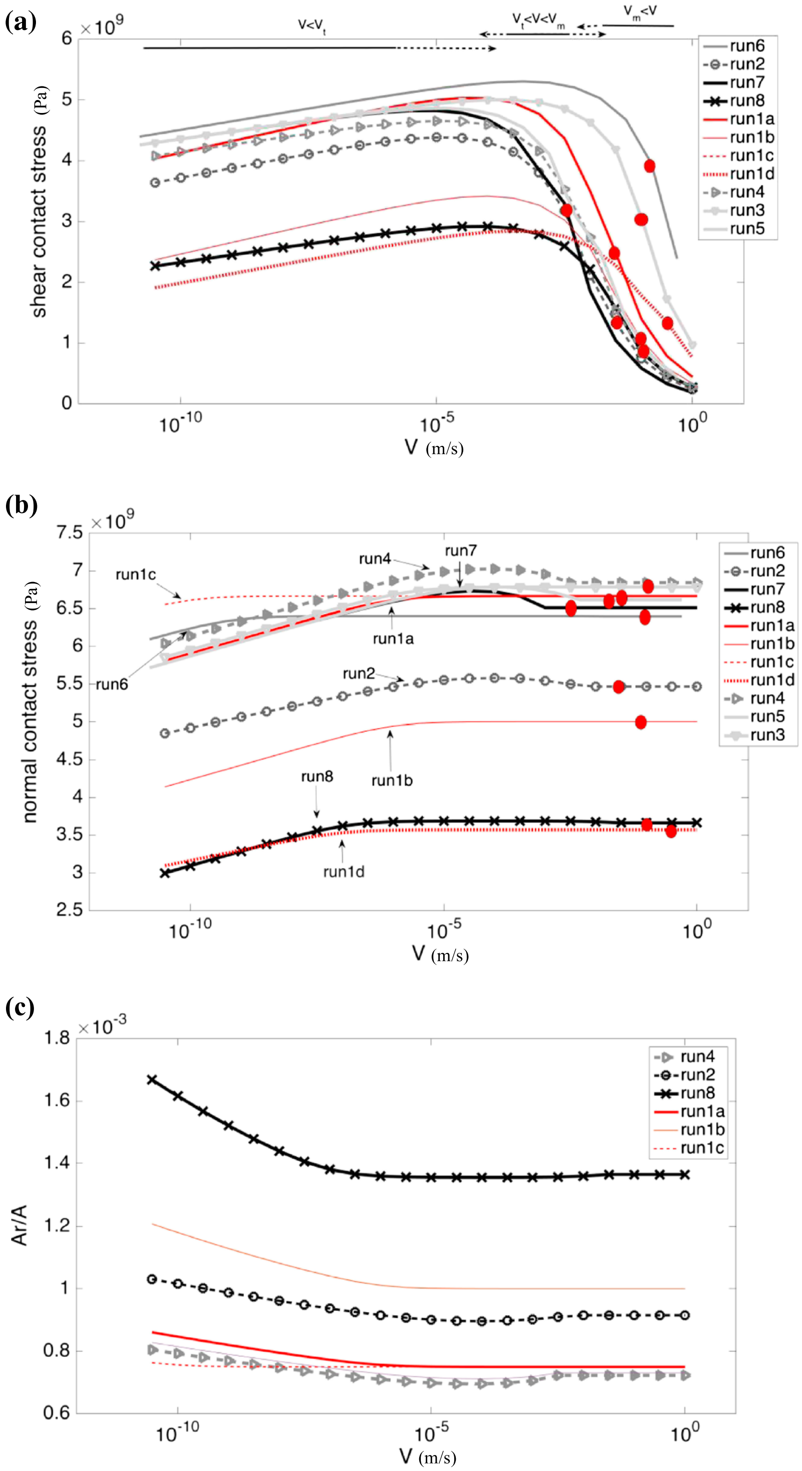

Figure 4. (a) Contact shear stress, τ_c, (b) normal stress, σ_c, and (c) normalized real contact area as function of V, at $T_0 = 30°\text{C}$, $\sigma_n = 5$ Mpa, for the runs detailed in Table 2. Onset of melting is marked by red circles. For $V < V_t$ ($\sim 10^{-5}$–10^{-4} m/s), τ_c is *V strengthening* in all runs due to the log term in equation (3b). For $V > V_t$, τ_c becomes strongly *V weakening* since thermal effects on coefficient *a* override the *V strengthening* of the log term in equation (3b) (see also discussion and equation (10)) (Figure 4a). After melting τ_c continues to drop. At low V, σ_c is *V strengthening* due to the increasingly limited time for contact growth during sliding (equation (3a)). *V strengthening* continues as long as contact lifetime, $t = d/V$, exceeds the cutoff time, t_c. At $V > V_c = d/t_c$ (V_c is marked by arrows for each curve), contact lifetime is smaller than t_c, so the *log* term in equation (3a) becomes negligible, and σ_c saturates to a nearly constant value (though minor changes can be seen for $V > V_t$). After melting, σ_c is assumed constant (Figure 4b). Real contact area (normalized by nominal contact area) changes appreciably only for slow V and remains approximately constant for $V > V_c$, at which point the contact area growth term (*b* term) becomes negligible (see equations (9a) and (9b)) (Figure 4c).

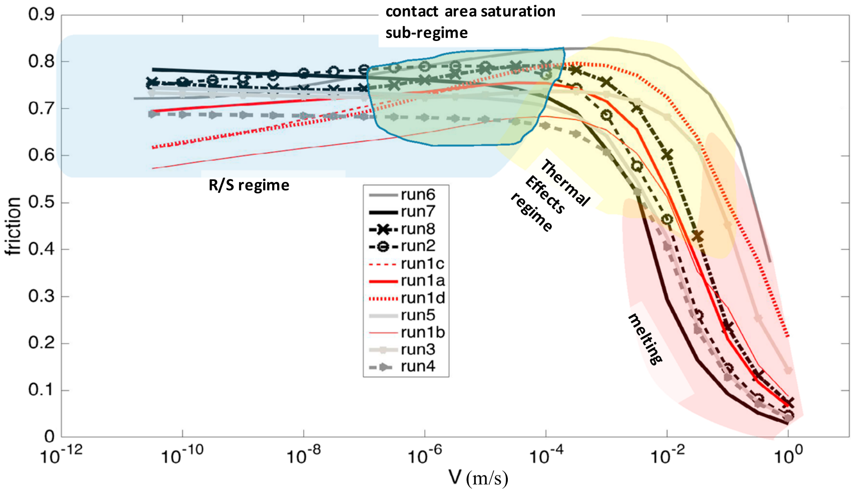

Figure 5. Model predictions (equation (4a)) for steady state friction coefficient, $\mu_{ss,}$ in quartz and granite as function of slip rate, V, for all runs in Table 2. Four main regimes of behavior are seen: At low V ($V < V_t$, where V_t is thermal velocity, blue region), μ_{ss} is temperature-independent and follows the traditional rate and state behavior (R/S). Here μ_{ss} may be either V weakening or V strengthening, depending on small variations in thermodynamic parameters. Within the R/S regime there is a subregime that starts at $V > V_c = d/t_c$, at which point contact area saturates (green region). In some cases, (runs 3 and 8), this causes a friction minimum followed by a peak, as observed sometimes in experiments (Figure 1). Figure 6c zooms into this regime in run 8. At high enough V ($V > V_t$, yellow region), thermal effects kick in (see Figure 3), causing a marked V weakening of friction. At even higher V, greater than V_m (red region), a transition to contact melting occurs (see Figure 3), with further friction reduction.

5.3. Friction Coefficient

The ratio between τ_c and σ_c (equation (4a)) provides the steady state friction coefficient, $\mu_{ss,}$ as function of V, plotted in Figure 5. Our model predicts four main regimes of friction, as shown in Figure 5, and illustrated by zooming into one of the runs in Figure 6.

1. Rate and state, at slowest shear rate, when shear heating is negligible, ($V < V_t$) friction is either velocity weakening or velocity strengthening (abbreviated V-W and V-S from here on). Whether friction is V-W or V-S in this regime depends on slight differences in parameter values: If contact normal stress, $\sigma_{c,}$ increases faster with V than contact shear stress τ_c does (e.g., note the different slopes of τ_c and σ_c in Figure 6b), the resulting ratio τ_c/σ_c produces V-W, and vice versa. We term this regime the *rate and state regime* since equation (4f) shows that the R/S description holds here as a first-order approximation. Note that all runs where $Q_v = Q_s$ (runs 1a–1d in Figure 5) show V-S behavior in this regime. V-W emerges only when Q_v differs from Q_s, and B differs from 1 (runs 3, 4, 5, 7, and 8 in Figure 5).
2. Minimum in friction, $V = V_c = d/t_c$. The R/S behavior either extends up to $V = V_t$ or can in some cases transition to a subregime. This subregime is characterized by a local *minimum of friction* within the R/S regime, at $V_c = d/t_{c.}$ We term V_c the *cutoff velocity* of the contact. Such a local minimum at V_c is seen in runs 8 and 3 of Figure 5. The minimum in friction of run 8 is shown more clearly in Figure 6. After the minimum, friction becomes V-S. The origin for the minimum is analyzed in section 6.
3. Maximum in friction, $V = V_t$. In systems that exhibit a minimum in friction (runs 3 and 8) or if friction is V-S in the R/S regime (e.g., runs 1a–1d in Figure 5) the R/S regime terminates at a maximum in friction. This maximum is not very evident in the data shown in Figure 1 but is commonly found in various materials under various conditions, as shown by Kohli et al. (2011, Figure 11), Bar-Sinai et al. (2014), and Spagnuolo et al. (2016) (monzonite in their Figure 2).
4. Shear heating at intermediate shear rate, $V_m > V > V_t$. Once V exceeds V_t, shear heating becomes significant and T starts rising precipitously in Figure 3. This regime is always V-W, since τ_c (Figure 4a) drops steeply with V, while σ_c is approximately constant with V (Figure 4b).
5. Melting at the highest shear rates, $V > V_m$, produces strong V-W, following equation (6), where τ_c drops as $1/\sqrt{V}$.

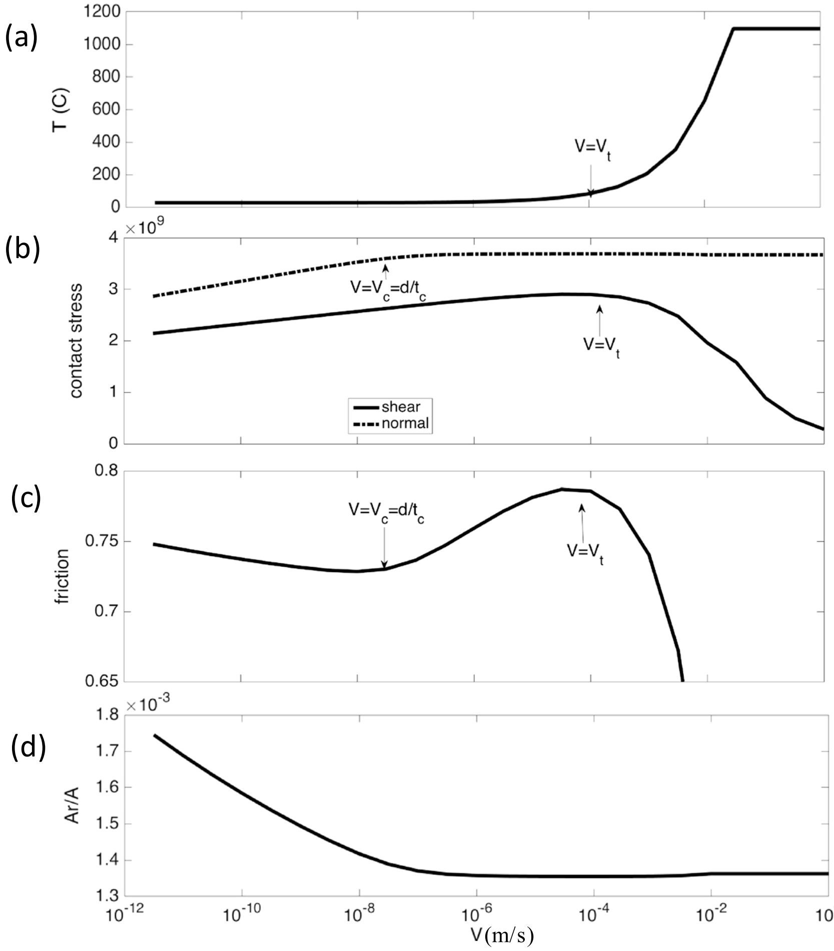

Figure 6. (a) Contact temperature, (b) contact shear and normal stresses (in Pa), (c) zoom into friction, and (d) normalized real contact area, from an example run, run 8. This run illustrates the main regimes and transition points between them, controlling friction in our model. At the low slip rate limit, it exemplifies a situation when velocity weakening at geological slip rates transitions to velocity strengthening at slightly higher slip rates (when $V > Vc = d/t_c$), due to the role that t_c plays in growth of real contact area A_r. At $V > V_c$ both A_r and σ_c saturate. Friction is then V strengthening, till the onset of thermal effects, at $V = V_t$. For $V > V_t$, shear heating causes thermal softening of shear stress and hence of friction.

To compare with experiments, the simulations from Figure 5 are replotted in Figure 7 together with the experimental data for quartzose rocks from Figure 1 (from Di Toro et al., 2011). The different model runs, which use a range of reasonable material parameters (as discussed in section 3 and summarized in Tables 1 and 2), predict and envelope the various behaviors observed experimentally in steady state sliding in quartz sandstone (Dieterich, 1978), granite (Di Toro et al., 2004; Dieterich, 1978), tonalite and tonalitic cataclasite, (Di Toro et al., 2006), and novaculite (Di Toro et al., 2004, 2006; Hirose and DiToro, unpublished, as reported in Figure 1 and supporting information of Di Toro et al. (2011)).

6. Discussion

The new model for steady state friction is conceptually simple: it assumes thermally activated creep of contacts, under coupled steady state stress and thermal conditions during sliding. The micromechanics model builds upon the works of, for example, Putelat et al. (2011), Rice et al. (2001), Nakatani and Scholz (2004b), Bowden and Tabor (1964), Baumberger and Caroli (2006), Brechet and Estrin (1994), and others but (1) adds steady state thermal effects, (2) relaxes nonphysical assumptions on yield stress σ_c^0, and (3) allows the activation energies and activation volumes to differ between shear and flattening creep processes. We also added a physical constraint to represent melting, assuming that once contacts reach melting they reduce stresses to

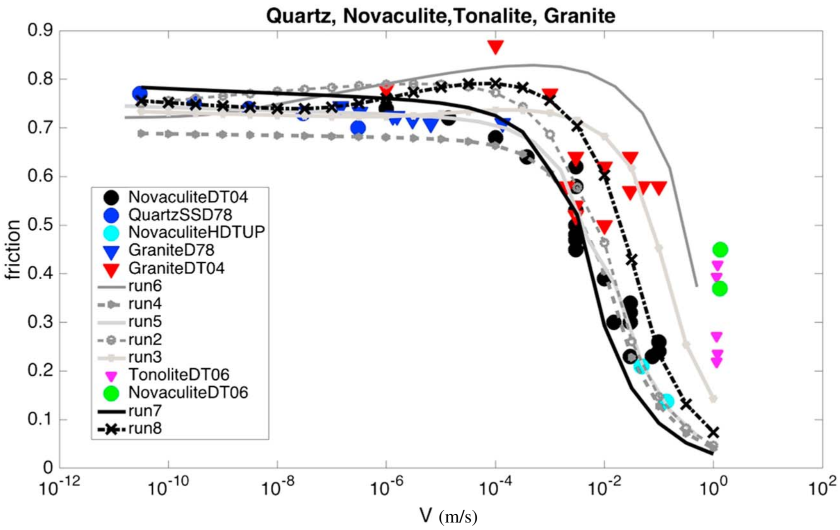

Figure 7. Modeling results for steady state friction, replotted from Figure 5, but now overlaid on top of the quartz sandstone, granite, novaculite, and tonalite experimental results that were presented in Figure 1 (from Di Toro et al., 2011). Our physics-based model results show excellent fit to experiments at all velocities and even predict the friction peak that is observed in some cases before the onset of melting. Experimental data (in symbols) is from shear experiments in tonalite and tonalitic cataclasite (Di Toro et al., 2006), novaculite (Di Toro et al., 2004, 2006; Hirose and DiToro, unpublished, as reported in Figure 1 and SM of DiToro et al., 2011), quartz sandstone (Dieterich, 1978), and granite (Di Toro et al., 2004; Dieterich, 1978).

remain at T_m. Thus, steady state is still maintained during melting, which means the molten zone is not widening with slip. We are not clear that this is a good assumption, but the focus here is not on melting, so we leave this for future work.

6.1. Comparison of Theory With Data

As shown in Figure 7 model results fit experiments well. Since all parameters are obtained independently or imposed externally, only a narrow play range was left for model fitting. Despite rather tight constrains on parameters, our model fits well and explains friction under a large range of velocity, temperature, and stress, for low temperature and normal stress experiments on quartz-rich rocks.

6.2. A Description of the Different Frictional Regimes

An example of the behavior predicted by our model is shown in Figure 6. It is in good agreement with experimental data, as shown in Figure 7. Here we provide a description of the phenomena responsible for the various types of behavior predicted and describe the relevant controlling parameters.

The velocity dependence of the stresses and friction in the low-velocity regime are determined by *a* and *b*, just as in conventional R/S friction (equation (4f)). Both contact shear and normal stresses are inherently velocity strengthening in the isothermal regime at low velocities (Figure 6b). Whether friction, the ratio of the stresses, is V-S or V-W depends on the relative rate of V-S of τ_c versus σ_c. For example, Figure 6b shows that in run 8 τ_c increases with *V* more slowly than does σ_c. This explains the V-W behavior of run 8 in the slow *V* regime, as seen in Figure 6c. (Note, however, that for the same run 8, *a*-*b* from equation (4f) do not predict V-W (see Table 2). This is because for this run, as in some cases, the expansion converges poorly and higher-order terms are required to calculate *a* and *b*, so the terms in equation (4g)) are insufficient to predict the velocity friction dependence. Thus, it is best to use the full equation (4a) for friction.)

The contact area, A_r/A, always decreases with velocity (Figure 6d)—this simply arises from the decrease in contact lifetime with *V*. However, when $V > V_c = d/t_c$, the rate at which A_r/A decreases with *V* slows and eventually ceases. This saturation of A_r leads to V-S friction with the rate parameter a' (the b' term in equation (4a) goes to zero, as will be derived below). If the friction was V-W at lower velocity, there may be a minimum in friction at $V = d/t_c$, as in run 8, Figure 6c. As seen in Figure 5, this subregime of R/S only appears in two of our runs, as it requires $V_c \ll V_t$. Similar behavior is observed in some other materials, for example, see Bar-Sinai et al. (2014, Figure 1).

At $V = V_t$, the contact temperature begins to rise rapidly with increasing slip rate, due to flash heating (Figure 6a). That causes the a' term in equation (4a) to become increasingly negative as V increases, leading τ_c to become strongly V-W. However, because A_r is already saturated, there is no such effect on σ_c, and friction becomes strongly V-W, resulting in a maximum in friction at V_t, as seen in Figure 6c.

This regime transitions to melting at a high V, $V > V_m$. V-W continues as τ_c drops to offset the shear heating that increases with V. This offset is required to attain constant T_c, so as to maintain our model-dictated steady state during melting.

6.3. Physical Interpretation of the Friction Coefficient

Three main coefficients emerge in this formalism as collections of material parameters, which control the physics of friction: a', b', and t_c.

6.3.1. The Viscous Shear Term

The a' term represents the ratio of contact temperature to shear activation energy and thus the material compliance to shear deformation—the higher a' is, the less resistance there is to shear deformation. The $a' \ln(V/V_{smax})$ term in equation (4a) arises from the τ_c equation, (3b). This term is always negative since $V < V_{smax}$. Since at low velocities a' is a positive constant and $\ln(V/V_{smax})$ becomes less negative with increasing V, τ_c increases with V at low velocities; hence, we call this a' term *the viscous shear term*. At higher velocities, where T_c increases, a' also increases accordingly (equation (4b)), resulting in thermal weakening of τ_c.

6.3.2. The Contact Area Growth Term

The b' term represents the ratio of contact temperature to volume creep activation energy and thus the material compliance to volume deformation. The higher b' is, the less resistance there is to compaction and flattening of the asperity. It is easier to understand the b' term in terms of A_r rather than from σ_c. The term $b'\ln(1 + d/(Vt_c))$ in equation (3c) is always positive, leading always to growth of A_r. Thus, we call this b' term the *contact-area growth term*. Increasing V reduces the growth of A_r because the load lifetime on contacts is reduced. When $V >> d/t_c$, then $\ln(1 + d/Vt_c) \rightarrow 0$. Thus, when $V \gg d/t_c$, both Ar and σ_c will saturate, as seen in Figures 4 and 6. In contrast to the a' term that changes considerably during shear heating, the b' term remains negligible even during shear heating (yet slight changes to A_r and σ_c are noticeable in Figures 4 and 6 at $V = V_t$). It will be demonstrated below that the b' term is only significant at slow V ($V \ll d/t_c$), while for $V \gg d/t_c$ it can be neglected, and A_r (and thus σ_c) can be taken as constant.

6.3.3. The Cutoff Time

The cutoff time, t_c, has a physical meaning that may be understood from evaluating the differential equation for contact normal stress, equation (2c), at time $t = 0$ and plugging in the definition of t_c from equation (2d), which gives

$$\left.\frac{d\sigma_c}{dt}\right|_{t=0} = -b'\frac{\sigma_c^0}{t_c} \tag{7}$$

Equation (7) says that t_c (modulated by b') is the combination of thermodynamic parameters, given by equation (2e), that controls the characteristic time for contact convergence and growth, at the time of contact formation ($t = 0$). Since t_c may be thermally activated (equation (2e)), the contact area growth rate, the rate of change in normal stress, and the rate of contact convergence are all thermally activated as well. In addition to its physical meaning, the cutoff time is a crucial parameter in controlling transitions between friction-velocity regimes, as shown in Ben David et al. (2010) and Marone (1998).

6.4. The Four Frictional Regimes and the Critical Velocities

Our simulations predict four sliding regimes as function of slip rate, where the transition between regimes is set by three critical slip rates. The first critical velocity is $V_c = d/t_c$, the "cutoff velocity" of the contact. The second-critical velocity, V_t, is the velocity above which substantial shear heating, and thus strong thermal weakening, takes place. The third critical slip rate is the one above which contacts melt, V_m. We find here that V_c ranges between 10^{-10} and 10^{-5} m/s, V_t ranges between 10^{-5} and 10^{-3} m/s, and V_m ranges between 10^{-3} and 10^{-1} m/s, depending on model parameters, mainly thermal diffusivity and contact size (see Figure 3 and Table 2). We next analyze friction dependence on velocity for these separate regimes.

6.4.1. Slow Sliding—the (*a-b*) Term and Frictional Stability

Equation (4f) shows that friction may be approximated in the slowest sliding regime, $V \ll V_c = d/t_c$, by the conventional R/S equation (1). In this regime the two behaviors of R/S, namely *V* weakening and *V* strengthening, arise in our model when applying small differences in thermodynamic parameters, within the material-allowed range. To see how V-S or V-W depend on material parameters, we differentiate equation (4f):

$$\frac{\partial \mu_{ss}}{\partial \ln(V)} \approx a - b = \mu_0 R T_c \left(\frac{1}{Q_s} - \frac{1}{BQ_v} \right) + \frac{(RT_c)^{2\mu_0}}{BQ_v} \left(\frac{1}{Q_s} \ln\left(\frac{dV_{s\max}}{t_c} \right) - \frac{2}{BQ_v} \ln\left(\frac{d}{t_c} \right) \right), \tag{8}$$

where the dependence of the *a* and *b* coefficients on material parameters is defined in equations (3d) and (4g)). The first equality of equation (8) predicts that when (*a-b*) > 0 friction is V-S, and when (*a-b*) < 0 friction is V-W. This prediction agrees with the standard interpretation of R/S laws (Marone, 1998). The predictions of equation (8), which are not material specific, also agree with the observations of Ikari et al. (2011) and Ikari et al. (2016) who find that in carbonates (*a-b*) depends linearly on the base friction μ_0, and that *a* and *b* have different linear dependence on μ_0 (Ikari et al., 2016, Figure 2c). This agrees with our definition of *a* and *b* (equation (4g)) that predicts that differences between *a* and *b* may result from a difference in values of Q_s and BQ_v or from the second-order corrections.

It is easy to show from equation (8) that when the activation energies are equal and $B = 1$, that is, when $Q_s = BQ_v$, friction is always V-S in this conventional R/S regime: The first parenthesis cancels out, while plugging in reasonable numbers shows that the second parenthesis is always positive. Indeed runs 1a–1d, which have $Q_s = Q_v$, show V-S in this R/S regime (Figure 5), independent of other parameter values.

The second-order corrections may play a crucial role even when $Q_s \neq Q_v$, if the first order is negative, but the second-order offsets it. Such a case is seen in run 6 for example (see Table 2). This is because although each of the first-order terms, *a* and *b*, may be relatively large on their own, their *difference* may be smaller than the second-order terms. In addition, for very small slip rate, the *b* term is large, and the $(\ln)^2$ term in equation (4d) may become important, as is the case for run 8. Run 8 has (*a-b*) > 0 but still shows V-W since the *b* term is large (*b* term increases for low-activation energy) and the accurate assessment requires addition of the $\ln^2 V$ term. Thus, although the R/S derivative equation (8) gives the correct stability criterion for friction in most cases, for accuracy it is best to use the full equation for friction, equation (4a).

Note also that equation (8) predicts a temperature dependence of (*a-b*): increasing ambient temperature will enhance the V-S or V-W that occurs at low *T*, by increasing the absolute value of (*a-b*). This prediction has implications for the depth of earthquake nucleation, which we shall leave for future studies.

6.4.2. Intermediate Sliding Rate—the Transition to Velocity Strengthening at $V > d/t_c$

The second sliding regime is actually a subregime of R/S. It emerges when the validity of the approximation in the low *V* R/S equation (4f) breaks down, that is, once *V* exceeds the cutoff velocity $V_c = d/t_c$, and we return to the primitive R/S approximation, equation (4b). Using the approximation that for small *x*, $\ln(1 + x) \sim x$. Equation (4b) predicts that friction in this regime is

$$\mu_{ss} \approx \mu_0 + a^* \ln\left(\frac{V}{V_{s\max}} \right) + b^* \frac{d}{Vt_c}, \tag{9a}$$

The size of the a^* and b^* terms can be evaluated as follows: on the one hand, for $V < 0.1$ m/s, $\left|\ln\left(\frac{V}{V_{s\max}}\right)\right| \sim 10$, on the other hand, in this regime $\frac{d}{Vt_c} < 1$. Since a^* is of the same order as b^* (Table 2), then the b^* term in equation (9a) is negligible relative to the a^* term, and equation (9a) can be approximated as

$$\mu_{ss} \approx \mu_0 + a^* \ln\left(\frac{V}{V_{s\max}} \right) \tag{9b}$$

which means that contact growth is not important in this regime, as is also seen in Figure 6, which shows that contact normal stress and area saturate for $V > V_c$.

In this regime, from equation (9b), $\frac{\partial \mu_{ss}}{\partial \ln(V)} \approx a^*$, which is always positive. Thus, *friction is always V strengthening in this R/S subregime of* $V_t \gg V \gg V_c$ (i.e., sliding rate that is still slow enough to not cause appreciable shear heating effects), *independent of the sign of* (*a-b*). Physically this is because contacts do not have time to grow when the velocity exceeds the cutoff velocity d/t_c, and in the absence of thermal effects (in this regime of still relatively slow slip), only the logarithmic V-S of the viscous term of τ_c prevails. This regime, however, only exists under certain conditions. For example, runs 4, 5, and 7 do not show a V-S portion of the curve because the window between $V_c < V < V_t$ shrinks in these runs (they have small t_c, large d, and relatively small V_t).

Cases where this regime exists, as in runs 3 and 8, show V-W at very low slip rate, followed by V-S at moderate slip rates (when $V > V_c$), and a transition to thermal softening at higher V, when $V > V_t$ (Figure 6c). A similar saddle-like behavior, causing a peak in friction, was experimentally observed in various materials (e.g., Kilgore et al., 1993; Shimamoto, 1986; Weeks & Tullis, 1985); Heslot et al., 1994), and its consequences have been discussed theoretically (Bar-Sinai et al., 2014; Noda, 2008), yet here we suggest the physics behind it. This issue of saddle-like behavior of friction reveals a basic behavior of friction that was largely overlooked in previous works. It stems from the control of d and t_c on a cutoff velocity and may be overlooked if one concentrates solely on the sign of a and b.

6.4.3. Fast Sliding—The Thermal Softening Regime at $V > V_t$

In the case of even faster slip rate, when V exceeds the thermal velocity V_t, the contacts heat up. At this fast velocity, certainly the condition of $V > d/t_c$ is met, and friction may be approximated by equation (9b). To analyze the dependence of friction on velocity, we differentiate equation (9b) with respect to V, but due to shear heating we account also for changes in a^* due to elevated contact temperature:

$$\frac{\partial \mu_{ss}}{\partial V} \sim \frac{a^*}{V} + \frac{\partial a^*}{\partial V} \ln\left(\frac{V}{V_{s\max}}\right) = \frac{a^*}{V} + \frac{\partial a^*}{\partial T_c}\frac{\partial T_c}{\partial V} \ln\left(\frac{V}{V_{s\max}}\right) = \frac{a^*}{V} + \frac{a^*}{V}\frac{T_c - T_0}{2T_c} \ln\left(\frac{V}{V_{s\max}}\right). \tag{10}$$

To obtain the last equality, we used $\frac{\partial T_c}{\partial V} = \frac{T_c - T_0}{2V}$ from equation (5) and $\frac{\partial a^*}{\partial T_c} = \frac{a^*}{T_c}$ from equation (4c). From the right-hand side (RHS) expression in equation (10) it is easy to see that friction thermally softens in this regime: the first term on the RHS is due to the regular velocity strengthening that is contributed by the viscous a^* coefficient and is always positive. The second term on the RHS comes from thermal softening. It is negative and much larger than the first term, causing overall softening. This is easily seen by plugging values: for example, for $V = 0.01$ m/s, $T_c \approx 250$°C (Figure 3). Plugging $V_{s\max}$ from Table 1 shows that the second term is negative, with a magnitude that is 2.5 times the first term. In short, thermal softening occurs because the thermal effect of the a^* coefficient overwhelms the velocity strengthening (viscous shear) effects of the logarithmic term.

6.4.4. Fastest Sliding—the Melting Regime at $V > V_m$

When contacts melt, equation (6) predicts that τ_c drops as $1/\sqrt{V}$. This is a consequence of the coupled steady state calculation of T and stresses. This drop is slower than the $\tau_c \sim 1/V$ predicted by the flash melting model of Rice (2006). The difference is since the flash melting model does not produce steady state. At this point we cannot say if steady state really occurs during melting in experiments or in nature. A possibly relevant aspect of the experimental high-velocity friction data is that the apparent steady state friction occurs in an "open system," that is, with gouge/melt flying out of the sample, which would not be the case in the Earth. This has been shown (Nielsen et al., 2008, 2010) to influence the dependence of friction on velocity in the $V > V_m$ regime. However, since melting is not the main issue of this study, we simply state these differences between models, and between experiments and nature.

6.5. The Importance of the Difference Between Volume Creep and Shear Creep

From equation (8), it is clear that the values and differences between the activation energies for contact flattening and surface shear are important for fault stability. The difference between shear and volume creep processes has not been dwelled upon previously, yet equation (8) predicts that $Q_s = BQ_v$ leads to V-S, while V-W will only emerge if Q_s is larger than BQ_v. This criterion can be met when $B < 1$, and/or when $Q_s < Q_v$. A difference in activation energies may arise from different processes controlling contact growth and shear, or from variations in structure as function of distance from contact, as discussed in section 3. The values of Q_s and Q_v are not accurately known at present. Possible ways to measure separately Q (and Ω) for surface and volume processes involve microindentation hardness experiments at varying temperature. Q_v may then be extracted from measurements of strain rate as function of t and T, following equation (3a). One can also measure a and b as function of temperature to extract the activation energies, as in Ikari et al. (2011, 2016). In that case fitted parameters at low V and T may be used to model the full phase space, namely the nonmonotonic friction as function of high V, T, and σ_n. A good fit across the full phase space, as obtained here, lends confidence to the validity of the model.

6.5.1. Constraining the Parameter Values

The original Bowden & Tabor paper (1950) concluded that because friction is τ_c/σ_c, the ratio of strength properties of the same material, the value of the friction coefficient should be independent of material. In geology this conclusion is known as Byerlee's law, which applies to all geological materials except for the laminar materials like phylosilicates (as was also recognized by B&T, 1964, chapter XI), which have unusual frictional properties. This conclusion of B&T (1950) agrees with our prediction: Q_s, BQ_v, Ω_s, and Ω_v determine μ_{ss} via τ_c and σ_c, and the absolute value of these depends on material. However, we find that their ratio should depend mainly on process and not on material.

We have constrained parameter values for our model based on thermodynamics measurements, as explained in section 3. Yet these parameters have a range of permissible values, as noted in Tables 1 and 2 and seen in Figures 5 and 7. One may further constrain these parameters within the allowable range, using experiments of friction and velocity trends. For this we concentrate on the friction coefficient at the limit of slow V, $V \ll d/t_c$, derived in equation (4f). In this very slow velocity regime, friction is V-W if (a-b) < 0, which requires $Q_s > BQ_v$. Since we know quartz is generally V-W, equation (4f) implies that in quartz the surface activation energy Q_s should be larger than BQ_v, the volumetric activation energy multiplied by constant B. We used this constraint in all runs, except for run 2 and runs 1a–1d, which were added for exploratory purposes. Another constraint, discussed in section 3, is that Q_v and Q_s in quartz are constrained by independent measures reported in the literature to be between 150 and 280 KJ/mol.

One may constrain Q_s, B, and Q_v further, by using experimental data of steady state values of (a-b). Marone (1998) compiled experiments on bare rock and gouge and finds steady state values of (a-b) for quartz, granite, and novaculite between 0 and -0.006. Runs 4, 5, and 7 show (a-b) values within the experimental range reported by Marone (1998) (see Table 2). These runs have relatively high activation energies, with $Q_s > Q_v + 30$ KJ/mol and $B < 1$. Although it is easy to find reasons why Q_v should differ from Q_s, it is less clear why Q_v should be smaller than Q_s.

An additional check for the parameters of the model is offered by the value of the real contact area, as seen in Figure 4c. In agreement with the experiments of Dieterich and Kilgore (1994), we obtain that $A_r/A \sim 10^{-3}$ at room temperature and low normal stress. The change of A_r with V, and its constancy for V exceeding d/t_c, can be tested in future experiments.

Finally, the parameters α_{therm} and d are independently constrained, as discussed in section 3. However, they are checked by V_t, the velocity at which thermal weakening initiates. V_t is observed by experiments (Figure 7) to be around 10^{-4}–10^{-3} m/s. This constrains the ratio d/α_{therm} from equation (5), assuming we know D_{th} from experiments.

6.6. Plastic Versus Brittle Behavior of Contacts

We have assumed that deformation at contacts, for what otherwise are considered brittle materials, is by low temperature plastic flow. Other models of rock friction have assumed brittle fracture at the contacts (e.g., Beeler, 2004). Such models produce similar results to ours because, as mentioned earlier, the velocity of subcritical crack growth depends exponentially on stress (Atkinson, 1987), similar to our equation (2a). Our assumption of contact-scale plasticity is based on the observation that for such materials, under static and moving loads, well-formed indentations and wear grooves are formed concordant with the indenting styli (Brace, 1963; Engelder & Scholz, 1976). This is explained because the high hydrostatic pressures that exist beneath contacts inhibit brittle fracture there (Bowden & Tabor, 1964, p.349; Evans & Goetze, 1979).

The wear detritus from rock friction is often dominated by angular fragments forming cataclasites. This indicates an important role for brittle fracture. The indentation experiments of Brace (1963) produced cone cracks surrounding the indents, and in the sliding styli experiments of Engelder and Scholz (1976) partial cone cracks were observed at the trailing edge of the styli tracks. Such cone cracks are predicted by the high tensile stresses that exist at the edges of contacts (Johnson, 1985 p. 94; Lawn, 1967). Thus, while plastic deformation at the contacts is the controlling process for friction, the growth of such cone cracks will lead to the plucking out of contacts, which will volumetrically dominate wear.

7. Conclusions

1. A physics-based model is proposed, based on the assumption of contact creep, to quantitatively predict steady state friction. The steady state is both of contact temperature and stresses at contacts. The model generalizes R/S friction and finds its physical basis. It provides a unifying physical basis that carries the same physics across all velocity scales. The a and b terms emerge as the viscous shear and contact growth terms, respectively.
2. The model explains and predicts the general observations of friction that are not material specific: (A) high friction and second-order velocity dependence at low V (conventional R/S friction law behavior). (B) Material dependent peak at intermediate velocity, just before onset of thermal effects. (C) Abrupt weakening above a critical velocity, termed V_t for thermal. At this velocity shear heating becomes meaningful. V_t is ~100 times slower than the velocity that produces contact melting. (D) All material dependencies result from variations in material properties that may be independently determined.
3. The model predicts four regimes of frictional behavior: R/S in its usual form, equation (1), is shown to be the low-velocity limit of our model, representing an end-member behavior on a continuum of the same physical behavior. In this regime fault stability is controlled in most cases by $\frac{\partial \mu_{ss}}{\partial \ln(V)} \approx a - b$ (although some cases require higher-order terms). Our model predicts three more experimentally observed regimes for frictional behavior, beyond the conventional R/S. The onset of the second regime is dictated by the cutoff time, t_c: When slip rate exceeds d/t_c, contacts cease to grow appreciably during sliding. This leads to contact area saturation and enhanced velocity strengthening. In this regime fault stability is controlled by the viscous shear term alone: $\frac{\partial \mu_{ss}}{\partial \ln(V)} = a^*$. This transition reveals the importance of the cutoff time t_c for friction. The third regime occurs at even faster sliding, when shear heating causes thermal softening. Thermal softening is achieved via thermal increase of the viscous shear a^* term (reducing friction since this term is negative). In this regime the b^* term is negligible, and fault stability is controlled by the dependence of the viscous shear term on shear heating: $\frac{\partial \mu_{ss}}{\partial V} \approx \frac{\partial a^*}{\partial T_c} \frac{\partial T_c}{\partial V} \ln\left(\frac{V}{V_{s\max}}\right)$. Friction calculation in this regime must thus be coupled with calculation of contact shear heating. The last regime occurs at the onset of contact melting and continues the weakening trend of the thermal softening regime.
4. The model predicts the importance of the difference between activation energies for shear and normal creep processes. The difference between these energies controls whether friction is velocity weakening or strengthening in the rate and state regime.

Acknowledgments
E. A. thanks H. Rubin, R. Toussaint, and J. Rice for helpful discussions. We thank G. Hirth and an anonymous reviewer for important comments that improved the manuscript considerably. EA is funded by ISF grant 910/17 The data and computer programs presented in this paper are available at http://en.earth.huji.ac.il/people/einat-aharonov.

References

Ashby, M. F., & Verrall, R. A. (1973). Diffusion accommodated flow and superplasticity. *Acta Metallurgica*, *21*(2), 149–163. https://doi.org/10.1016/0001-6160(73)90057-6

Atkinson, B. K. (1987). Introduction to fracture mechanics and its geophysical applications. In B. K. Atkinson (Ed.), *Fracture mechanics of rock*, (pp. 1–26). London: Academic Press. https://doi.org/10.1016/B978-0-12-066266-1.50006-5

Bar-Sinai, Y., Spatschek, R., Brener, E. A., & Bouchbinder, E. (2014). On the velocity-strengthening behavior of dry friction. *Journal of Geophysical Research: Solid Earth*, *119*, 1738–1748. https://doi.org/10.1002/2013JB010586

Baumberger, T. (1997). Contact dynamics and friction at a solid-solid interface: Material versus statistical aspects. *Solid State Communications*, *102*, 175–185.

Baumberger, T., & Caroli, C. (2006). Solid friction from stick–slip down to pinning and aging. *Advances in Physics*, *55*(3-4), 279–348. https://doi.org/10.1080/00018730600732186

Beeler, N. M. (2004). Review of the physical basis of laboratory-derived relations for brittle failure and their implications for earthquake occurrence and earthquake nucleation. *Pure and Applied Geophysics*, *161*(9–10), 1853–1876. https://doi.org/10.1007/s00024-004-2536-z

Beeler, N. M., Tullis, T. E., & Goldsby, D. L. (2008). Constitutive relationships and physical basis of fault strength due to flash heating. *Journal of Geophysical Research*, *113*, B01401. https://doi.org/10.1029/2007JB004988

Ben-David, O., Rubinstein, S. M., & Fineberg, J. (2010). Slip-stick and the evolution of frictional strength. *Nature*, *463*(7277), 76–79. https://doi.org/10.1038/nature08676

Berthoud, P., Baumberger, T., G'sell, C., & Hiver, J. M. (1999). Physical analysis of the state-and rate-dependent friction law: Static friction. *Physical Review B*, *59*(22), 14,313–14,327. https://doi.org/10.1103/PhysRevB.59.14313

Blanpied, M. L., Lockner, D. A., & Byerlee, J. D. (1995). Frictional slip of granite at hydrothermal conditions. *Journal of Geophysical Research*, *100*(B7), 13,045–13,064. https://doi.org/10.1029/95JB00862

Boettcher, M. S., Hirth, G., & Evans, B. (2007). Olivine friction at the base of oceanic seismogenic zones. *Journal of Geophysical Research*, *112*, B01205. https://doi.org/10.1029/2006JB004301

Boitnott, G. N., Biegel, R. L., Scholz, C. H., Yoshioka, N., & Wang, W. (1992). Micromechanics of rock friction 2: Quantitative modeling of initial friction with contact theory. *Journal of Geophysical Research*, *97*(B6), 8965–8978.

Bowden, F. P., & Tabor, D. (1950). *The friction and lubrication of solids (Vol. 1, No. 1)*. Oxford: Clarendon press.

Bowden, F. P., & Tabor, D. (1964). *The friction and lubrication of solids (Vol. 2, No. 2)*. Oxford: Clarendon press.

Brace, W. F. (1963). Behavior of quartz during indentation. *Journal of Geology*, *71*(5), 581–595. https://doi.org/10.1086/626934

Braeck, S., & Podladchikov, Y. Y. (2007). Spontaneous thermal runaway as an ultimate failure mechanism of materials. *Physical Review Letters*, *98*(9), 095504. https://doi.org/10.1103/PhysRevLett.98.095504

Brechet, Y., & Estrin, Y. (1994). The effect of strain rate sensitivity on dynamic friction of metals. *Scripta Metallugica et Materialia*, *30*(11), 1449–1454. https://doi.org/10.1016/0956-716X(94)90244-5

Brown, K. M., & Fialko, Y. (2012). Melt-welt mechanism of extreme weakening of gabbro at seismic slip rates. *Nature*, *488*(7413), 638–641. https://doi.org/10.1038/nature11370

Carpenter, B. M., Collettini, C., Viti, C., & Cavallo, A. (2016). The influence of normal stress and sliding velocity on the frictional behaviour of calcite at room temperature: Insights from laboratory experiments and microstructural observations. *Geophysical Journal International*, *205*(1), 548–561. https://doi.org/10.1093/gji/ggw038

Chen, X., Madden, A. S., Bickmore, B. R., & Reches, Z. E. (2013). Dynamic weakening by nanoscale smoothing during high-velocity fault slip. *Geology*, *41*(7), 739–742. https://doi.org/10.1130/G34169.1

Chester, F. M. (1994). Effects of temperature on friction: Constitutive equations and experiments with quartz gouge. *Journal of Geophysical Research*, *99*(B4), 7247–7261. https://doi.org/10.1029/93JB03110

Chester, F. M., & Higgs, N. G. (1992). Multimechanism friction constitutive model for ultrafine quartz gouge at hypocentral conditions. *Journal of Geophysical Research*, *97*(B2), 1859–1870. https://doi.org/10.1029/91JB02349

De Paola, N., Holdsworth, R. E., Viti, C., Collettini, C., & Bullock, R. (2015). Can grain size sensitive flow lubricate faults during the initial stages of earthquake propagation? *EPSL*, *431*, 48–58. https://doi.org/10.1016/j.epsl.2015.09.002

den Hartog, S. A., Peach, C. J., de Winter, D. M., Spiers, C. J., & Shimamoto, T. (2012). Frictional properties of megathrust fault gouges at low sliding velocities: New data on effects of normal stress and temperature. *Journal of Structural Geology*, *38*, 156–171. https://doi.org/10.1016/j.jsg.2011.12.001

Di Toro, G., Goldsby, D. L., & Tullis, T. E. (2004). Friction falls towards zero in quartz rock as slip velocity approaches seismic rates. *Nature*, *427*(6973), 436–439. https://doi.org/10.1038/nature02249

Di Toro, G., Hirose, T., Nielsen, S., Pennacchioni, G., & Shimamoto, T. (2006). Natural and experimental evidence of melt lubrication of faults during earthquakes. *Science*, *311*(5761), 647–649. https://doi.org/10.1126/science.1121012

Di Toro, G., Hirose, T., Nielsen, S., & Shimamoto, T. (2006). Relating high-velocity rock friction experiments to coseismic slip. In R. Abercrombie, et al. (Eds.), *Radiated energy and the physics of faulting*, *Geophysical Monograph Series* (Vol. 170, pp. 121–134). Washington, DC: American Geophysical Union. https://doi.org/10.1029/170GM13

Di Toro, G., Han, R., Hirose, T., De Paola, N., Nielsen, S., Mizoguchi, K., … Shimamoto, T. (2011). Fault lubrication during earthquakes. *Nature*, *471*(7339), 494–498. https://doi.org/10.1038/nature09838

Dieterich, J. H. (1972). Time-dependent friction in rocks. *Journal of Geophysical Research*, *77*(20), 3690–3697. https://doi.org/10.1029/JB077i020p03690

Dieterich, J. H. (1978). Time-dependent friction and the mechanics of stick-slip. *Pure and Applied Geophysics*, *116*(4-5), 790–806. https://doi.org/10.1007/BF00876539

Dieterich, J. H. (1979). Modeling of rock friction: 1. Experimental results and constitutive equations. *Journal of Geophysical Research*, *84*(B5), 2161–2168. https://doi.org/10.1029/JB084iB05p02161

Dieterich, J. H., & Kilgore, B. D. (1994). Direct observation of frictional contacts—New insights for state-dependent properties. *Pure and Applied Geophysics*, *143*(1-3), 283–302. https://doi.org/10.1007/BF00874332

Dieterich, J. H., & Kilgore, B. (1996). Implications of fault constitutive properties for earthquake prediction. *Proceedings of the National Academy of Sciences of the United States of America*, *93*(9), 3787–3794. https://doi.org/10.1073/pnas.93.9.3787

Engelder, T., & Scholz, C. H. (1976). The role of asperity indentation and ploughing in rock friction—II. Influence of relative hardness and normal load. *International Journal of Rock Mechanics and Mining Science and Geomechanics*, *13*(5), 155–163. https://doi.org/10.1016/0148-9062(76)90820-2

Evans, B. (1984). The effect of temperature and impurity content on indentation hardness of quartz. *Journal of Geophysical Research*, *89*(B6), 4213–4222. https://doi.org/10.1029/JB089iB06p04213

Evans, B., & Goetze, C. (1979). The temperature variation of hardness of olivine and its implication for polycrystalline yield stress. *Journal of Geophysical Research*, *84*(B10), 5505–5524. https://doi.org/10.1029/JB084iB10p05505

Faulkner, D. R., Mitchell, T. M., Behnsen, J., Hirose, T., & Shimamoto, T. (2011). Stuck in the mud? Earthquake nucleation and propagation through accretionary forearcs. *Geophysical Research Letters*, *38*, L18303. https://doi.org/10.1029/2011GL048552

Ferri, F., Di Toro, G., Hirose, T., & Shimamoto, T. (2010). Evidences of thermal pressurization in high velocity friction experiments on smectite-rich gouges. *Terra Nova*, *22*(5), 347–353. https://doi.org/10.1111/j.1365-3121.2010.00955.x

Gibert, B., & Mainprice, D. (2009). Effect of crystal preferred orientations on the thermal diffusivity of quartz polycrystalline aggregates at high temperature. *Tectonophysics*, *465*(1-4), 150–163. https://doi.org/10.1016/j.tecto.2008.11.006

Goldsby, D. L., & Tullis, T. E. (2002). Low frictional strength of quartz rocks at subseismic slip rates. *Geophysical Research Letters*, *29*(17), 1844. https://doi.org/10.1029/2002GL015240

Goldsby, D. L., & Tullis, T. E. (2011). Flash heating leads to low frictional strength of crustal rocks at earthquake slip rates. *Science*, *334*(6053), 216–218. https://doi.org/10.1126/science.1207902

Goren, L., & Aharonov, E. (2007). Long runout landslides: The role of frictional heating and hydraulic diffusivity. *Geophysical Research Letters*, *34*, L07301. https://doi.org/10.1029/2006GL028895

Goren, L., & Aharonov, E. (2009). On the stability of landslides: A thermo-poro-elastic approach. *Earth and Planetary Science Letters*, *277*(3-4), 365–372. https://doi.org/10.1016/j.epsl.2008.11.002

Goren, L., Aharonov, E., & Anders, M. H. (2010). The long runout of the Heart Mountain landslide: Heating, pressurization, and carbonate decomposition. *Journal of Geophysical Research*, *115*, B10210. https://doi.org/10.1029/2009JB007113

Green, H. W. II, Shi, F., Bozhilov, K., Xia, G., & Reches, Z. (2015). Phase transformation and nanometric flow cause extreme weakening during fault slip. *Nature Geoscience*, *8*(6), 484–489. https://doi.org/10.1038/ngeo2436

Hanley, E. J., Dewitt, D. P., & Roy, R. F. (1978). The thermal diffusivity of eight well-characterized rocks for the temperature range 300–1000 K. *Engineering Geology*, *12*, 31–47. https://doi.org/10.1016/0013-7952(78)90003-0

Heslot, F., Baumberger, T., Perrin, B., Caroli, B., & Caroli, C. (1994). Creep, stick-slip, and dry friction dynamics: Experiments and a heuristic model. *Physical Review E*, *49*(6), 4973–4988. https://doi.org/10.1103/PhysRevE.49.4973

Ikari, M. J., Marone, C., & Saffer, D. M. (2011). On the relation between fault strength and frictional stability. *Geology*, *39*(1), 83–86. https://doi.org/10.1130/G31416.1

Ikari, M. J., Carpenter, B. M., & Marone, C. (2016). A microphysical interpretation of rate-and state-dependent friction for fault gouge. *Geophysics, Geosystems, Geochemistry*, *17*, 1660–1677. https://doi.org/10.1002/2016GC006286

Jaoul, O., Tullis, J., & Kronenberg, A. (1984). The effect of varying water contents on the creep behavior of Heavitree quartzite. *Journal of Geophysical Research*, *89*(B6), 4298–4312. https://doi.org/10.1029/JB089iB06p04298

Johnson, K. L. (1985). *Contact mechanics*. Cambridge: Cambridge University Press. https://doi.org/10.1017/CBO9781139171731

Kelemen, P. B., & Hirth, G. (2007). A periodic shear-heating mechanism for intermediate-depth earthquakes in the mantle. *Nature*, *446*(7137), 787–790. https://doi.org/10.1038/nature05717

Kilgore, B. D., Blanpied, M. L., & Dieterich, J. H. (1993). Velocity dependent friction of granite over a wide range of conditions. *Geophysical Research Letters*, *20*(10), 903–906.

Kirby, S. H., & Kronenberg, A. K. (1987). Rheology of the lithosphere: Selected topics. *Reviews of Geophysics*, *25*(6), 1219–1244. https://doi.org/10.1029/RG025i006p01219

Kirkpatrick, J. D., Rowe, C. D., White, J. C., & Brodsky, E. E. (2013). Silica gel formation during fault slip: Evidence from the rock record. *Geology*, *41*(9), 1015–1018. https://doi.org/10.1130/G34483.1

Kohli, A. H., Goldsby, D. L., Hirth, G., & Tullis, T. (2011). Flash weakening of serpentinite at near-seismic slip rates. *Journal of Geophysical Research*, *116*, B03202. https://doi.org/10.1029/2010JB007833

Lawn, B. R. (1967). Partial cone crack formation in a brittle material loaded with a sliding spherical indenter. *Proceedings of the Royal Society of London Series A*, *299*(1458), 307–316. https://doi.org/10.1098/rspa.1967.0138

Li, T., & Rubin, A. M. (2017). A microscopic model of rate and state friction evolution. *Journal of Geophysical Research: Solid Earth*, *122*, 6431–6453. https://doi.org/10.1002/2017JB013970

Lockner, D. A., Summers, R., & Byerlee, J. D. (1986). Effects of temperature and sliding rate on frictional strength of granite. *Pure and Applied Geophysics*, *124*(3), 445–469. https://doi.org/10.1007/BF00877211

Mainprice, D., & Jaoul, O. (2009). A transmission electron microscopy study of experimentally deformed quartzite with different degrees of doping. *Physics of the Earth and Planetary Interiors*, *172*(1-2), 55–66. https://doi.org/10.1016/j.pepi.2008.07.009

Marone, C. (1998). Laboratory-derived friction laws and their application to seismic faulting. *Annual Review of Earth and Planetary Sciences*, *26*(1), 643–696. https://doi.org/10.1146/annurev.earth.26.1.643

Marone, C., & Scholz, C. (1988). The depth of seismic faulting and the upper transition from stable to unstable slip regimes. *Geophysical Research Letters*, *15*(6), 621–624. https://doi.org/10.1029/GL015i006p00621

Nakatani, M. (2001). Conceptual and physical clarification of rate and state friction: Frictional sliding as a thermally activated rheology. *Journal of Geophysical Research*, *106*(B7), 13,347–13,380. https://doi.org/10.1029/2000JB900453

Nakatani, M., & Scholz, C. H. (2004a). Frictional healing of quartz gouge under hydrothermal conditions: 1. Experimental evidence for solution transfer healing mechanism. *Journal of Geophysical Research*, *109*, B07201. https://doi.org/10.1029/2001JB001522

Nakatani, M., & Scholz, C. H. (2004b). Frictional healing of quartz gouge under hydrothermal conditions: 2. Quantitative interpretation with a physical model. *Journal of Geophysical Research*, *109*, B07202. https://doi.org/10.1029/2003JB002938

Nielsen, S., Di Toro, G., Hirose, T., & Shimamoto, T. (2008). Frictional melt and seismic slip. *Journal of Geophysical Research*, *113*, B01308. https://doi.org/10.1029/2007JB005122

Nielsen, S., Mosca, P., Giberti, G., Di Toro, G., Hirose, T., & Shimamoto, T. (2010). On the transient behavior of frictional melt during seismic slip. *Journal of Geophysical Research*, *115*, B10301. https://doi.org/10.1029/2009JB007020

Noda, H. (2008). Frictional constitutive law at intermediate slip rates accounting for flash heating and thermally activated slip process. *Journal of Geophysical Research*, *113*, B09302. https://doi.org/10.1029/2007JB005406

Noda, H., & Lapusta, N. (2013). Stable creeping fault segments can become destructive as a result of dynamic weakening. *Nature*, *493*(7433), 518–521. https://doi.org/10.1038/nature11703

Perfettini, H., & Molinari, A. (2017). A micromechanical model of rate and state friction: 1. Static and dynamic sliding. *Journal of Geophysical Research: Solid Earth*, *122*, 2590–2637. https://doi.org/10.1002/2016JB013302.

Platt, J. D., Rudnicki, J. W., & Rice, J. R. (2014). Stability and localization of rapid shear in fluid-saturated fault gouge: 2. Localized zone width and strength evolution. *Journal of Geophysical Research: Solid Earth*, *119*, 4334–4359. https://doi.org/10.1002/2013JB010711

Platt, J. D., Brantut, N., & Rice, J. R. (2015). Strain localization driven by thermal decomposition during seismic shear. *Journal of Geophysical Research: Solid Earth*, *120*, 4405–4433. https://doi.org/10.1002/2014JB011493

Poirier, J. P. (1985). *Creep of crystals: High-temperature deformation processes in metals, ceramics and minerals*. Cambridge, UK: Cambridge University Press. https://doi.org/10.1017/CBO9780511564451

Proctor, B. P., Mitchell, T. M., Hirth, G., Goldsby, D., Zorzi, F., Platt, J. D., & Di Toro, G. (2014). Dynamic weakening of serpentinite gouges and bare surfaces at seismic slip rates. *Journal of Geophysical Research: Solid Earth*, *119*, 8107–8131. https://doi.org/10.1002/2014JB011057

Putelat, T., Dawes, J. H., & Willis, J. R. (2011). On the microphysical foundations of rate-and-state friction. *Journal of the Mechanics and Physics of Solids*, *59*(5), 1062–1075. https://doi.org/10.1016/j.jmps.2011.02.002

Reches, Z. E., & Lockner, D. A. (2010). Fault weakening and earthquake instability by powder lubrication. *Nature*, *467*(7314), 452–455. https://doi.org/10.1038/nature09348

Rice, J. R. (2006). Heating and weakening of faults during earthquake slip. *Journal of Geophysical Research*, *111*, B05311. https://doi.org/10.1029/2005JB004006

Rice, J. R., Lapusta, N., & Ranjith, K. (2001). Rate and state dependent friction and the stability of sliding between elastically deformable solids. *Journal of the Mechanics and Physics of Solids*, *49*(9), 1865–1898. https://doi.org/10.1016/S0022-5096(01)00042-4

Rubinstein, S. M., Cohen, G., & Fineberg, J. (2004). Detachment fronts and the onset of dynamic friction. *Nature*, *430*(7003), 1005–1009. https://doi.org/10.1038/nature02830

Ruina, A. (1983). Slip instability and state variable friction laws. *Journal of Geophysical Research*, *88*(10), 359–310.

Scholz, C. H. (1972). Static fatigue of quartz. *Journal of Geophysical Research*, *77*(11), 2104–2114. https://doi.org/10.1029/JB077i011p02104

Scholz, C. H. (1988). The brittle-plastic transition and the depth of seismic faulting. *Geologische Rundschau*, *77*(1), 319–328. https://doi.org/10.1007/BF01848693

Scholz, C. H. (1998). Earthquakes and friction laws. *Nature*, *391*(6662), 37–42. https://doi.org/10.1038/34097

Scholz, C. H. (2002). *The mechanics of earthquakes and faulting*. Cambridge, UK: Cambridge University Press. https://doi.org/10.1017/CBO9780511818516

Scholz, C. H., & Engelder, T. (1976). Role of asperity indentation and ploughing in rock friction. *International Journal of Rock Mechanics and Mining Sciences*, *13*(5), 149–154. https://doi.org/10.1016/0148-9062(76)90819-6

Scholz, C. H., Molnar, P., & Johnson, T. (1972). Detailed studies of frictional sliding of granite and implications for earthquake mechanism. *Journal of Geophysical Research*, *77*(32), 6392–6406. https://doi.org/10.1029/JB077i032p06392

Shimamoto, T. (1986). Transition between frictional slip and ductile flow for halite shear zones at room temperature. *Science*, *231*(4739), 711–714. https://doi.org/10.1126/science.231.4739.711

Shimamoto, T., & Noda, H. (2014). A friction to flow constitutive law and its application to a 2-D modeling of earthquakes. *Journal of Geophysical Research: Solid Earth*, *119*, 8089–8106. https://doi.org/10.1002/2014JB011170

Siman-Tov, S., Aharonov, E., Sagy, A., & Emmanuel, S. (2013). Nanograins form carbonate fault mirrors. *Geology*, *41*(6), 703–706. https://doi.org/10.1130/G34087.1

Siman-Tov, S., Aharonov, E., Boneh, Y., & Reches, Z. E. (2015). Fault mirrors along carbonate faults: Formation and destruction during shear experiments. *Earth and Planetary Science Letters*, *430*, 367–376. https://doi.org/10.1016/j.epsl.2015.08.031

Spagnuolo, E., Nielsen, S., Violay, M., & Di Toro, G. (2016). An empirically-based steady-state friction law and implications for fault stability. *Geophysical Research Letters*, *43*, 3263–3271. https://doi.org/10.1002/2016GL067881

Sulem, J., & Famin, V. (2009). Thermal decomposition of carbonates in fault zones: Slip-weakening and temperature-limiting effects. *Journal of Geophysical Research*, *114*, B06311. https://doi.org/10.1029/2009JB006576

Tsenn, M. C., & Carter, N. L. (1987). Upper limits of power law creep of rocks. *Tectonophysics*, *136*(1-2), 1–26. https://doi.org/10.1016/0040-1951(87)90332-5

Van Diggelen, E. W., De Bresser, J. H., Peach, C. J., & Spiers, C. J. (2010). High shear strain behaviour of synthetic muscovite fault gouges under hydrothermal conditions. *Journal of Structural Geology*, *32*(11), 1685–1700. https://doi.org/10.1016/j.jsg.2009.08.020

Verberne, B. A., Spiers, C. J., Niemeijer, A. R., De Bresser, J. H. P., De Winter, D. A. M., & Plümper, O. (2014). Frictional properties and microstructure of calcite-rich fault gouges sheared at sub-seismic sliding velocities. *Pure and Applied Geophysics*, *171*(10), 2617–2640. https://doi.org/10.1007/s00024-013-0760-0

Verberne, B. A., Plümper, O., de Winter, D. M., & Spiers, C. J. (2014). Superplastic nanofibrous slip zones control seismogenic fault friction. *Science*, *346*(6215), 1342–1344. https://doi.org/10.1126/science.1259003

Verberne, B. A., Niemeijer, A. R., De Bresser, J. H., & Spiers, C. J. (2015). Mechanical behavior and microstructure of simulated calcite fault gouge sheared at 20–600°C: Implications for natural faults in limestone. *Journal of Geophysical Research: Solid Earth*, *120*, 8169–8196. https://doi.org/10.1002/2015JB012292

Vosteen, H. D., & Schellschmidt, R. (2003). Influence of temperature on thermal conductivity, thermal capacity and thermal diffusivity for different types of rock. *Physics and Chemistry of the Earth, Parts A/B/C*, *28*(9-11), 499–509. https://doi.org/10.1016/S1474-7065(03)00069-X

Weeks, J. D., & Tullis, T. E. (1985). Frictional sliding of dolomite: A variation in constitutive behavior. *Journal of Geophysical Research*, *90*(B9), 7821–7826. https://doi.org/10.1029/JB090iB09p07821

Wiederhorn, S. M., & Bolz, L. H. (1970). Stress corrosion and static fatigue of glass. *Journal of the American Ceramic Society*, *53*(10), 543–548. https://doi.org/10.1111/j.1151-2916.1970.tb15962.x

Yao, L., Ma, S., Niemeijer, A. R., Shimamoto, T., & Platt, J. D. (2016). Is frictional heating needed to cause dramatic weakening of nanoparticle gouge during seismic slip? Insights from friction experiments with variable thermal evolutions. *Geophysical Research Letters*, *43*, 6852–6860. https://doi.org/10.1002/2016GL069053